MCAT Institute
Final Report
95-11

Computational Analysis of Forebody Tangential Slot Blowing on the High Alpha Research Vehicle

Ken Gee

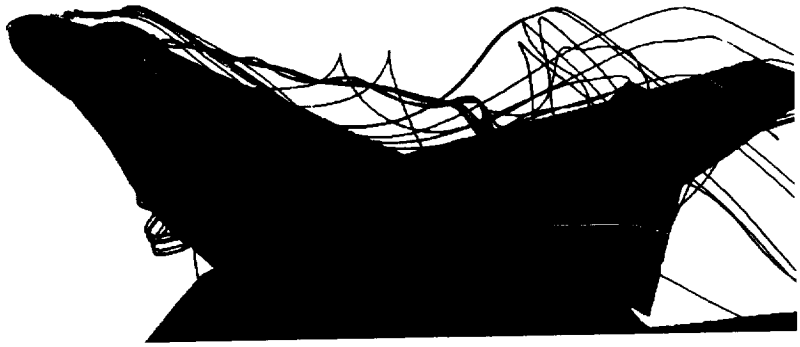

January 1995

NCC2-657

MCAT Institute
3933 Blue Gum Drive
San Jose, CA 95127

COMPUTATIONAL ANALYSIS OF FOREBODY TANGENTIAL SLOT BLOWING ON THE HIGH ALPHA RESEARCH VEHICLE

FINAL REPORT FOR GRANT NCC2-657

Ken Gee,
Principal Investigator
MCAT Institute
Moffett Field, CA 94035

Abstract

A numerical analysis of forebody tangential slot blowing as a means of generating side force and yawing moment is conducted using an aircraft geometry. The Reynolds-averaged, thin-layer, Navier-Stokes equations are solved using a partially flux-split, approximately-factored algorithm. An algebraic turbulence model is used to determine the turbulent eddy viscosity values. Solutions are obtained using both patched and overset grid systems. In the patched grid model, an actuator plane is used to introduce jet variables into the flow field. The overset grid model is used to model the physical slot geometry and facilitate modeling of the full aircraft configuration. A slot optimization study indicates that a short slot located close to the nose of the aircraft provided the most side force and yawing moment per unit blowing coefficient. Comparison of computed surface pressure with that obtained in full-scale wind tunnel tests produce good agreement, indicating the numerical method and grid system used in the study are valid. Full aircraft computations resolve the changes in vortex burst point due to blowing. A time-accurate full-aircraft solution shows the effect of blowing on the changes in the frequency of the aerodynamic loads over the vertical tails. A study of the effects of freestream Mach number and various jet parameters indicates blowing remains effective through the transonic Mach range. An investigation of the force onset time lag associated with forebody blowing shows the lag to be minimal. The knowledge obtained in this study may be applied to the design of a forebody tangential slot blowing system for use on flight aircraft.

Introduction

Survival of fighter aircraft in present and future air combat requires expansion of the flight envelope into regions that have heretofore been unattainable. This includes being capable of controlled flight at high angles of attack. Being able to maneuver at high angles of attack will give the fighter pilot the ability to engage his weapons systems faster and to outmaneuver his opponent. However, flight at high angles of attack presents a unique set of control problems.

The behavior of aircraft flying at high angle of attack is being studied by the NASA High Alpha Technology Program. This study includes flight tests,[1] wind tunnel experiments,[2] and computational fluid dynamics (CFD) simulations.[3,4] The flight vehicle used in the program is the High Alpha Research Vehicle (HARV). The HARV is a highly instrumented F/A-18, a current generation fighter aircraft. Surface pressure data and smoke flow visualizations have been obtained from the flight tests in order to understand the behavior of the flow field. These results, along with data obtained from the wind tunnel tests, have been used to validate the CFD analysis. The CFD results, in turn, has provided a detailed picture of the flow field behavior.

The flow about an aircraft flying at high angle of attack is characterized by large vortices formed by separated flow from the fuselage forebody and wings (Fig. 1). As the aircraft pitches up, the control power of the vertical tails is reduced as the tails are immersed in the low-energy wake flow of the wings and fuselage. However, the control power required by the aircraft to maintain directional stability increases with angle of attack. This is due to the asymmetry that arises in the vortical flow field over the forebody. Adding to the control problem is the propensity of the vortices to burst at the higher angles of attack. The asymmetry in the flow field and the bursting of the vortices may create large side force and yawing moments, leading to departure from the intended flight path. In order to maintain control of the aircraft flying at high angles of attack, new methods must be developed to provide the necessary control power.

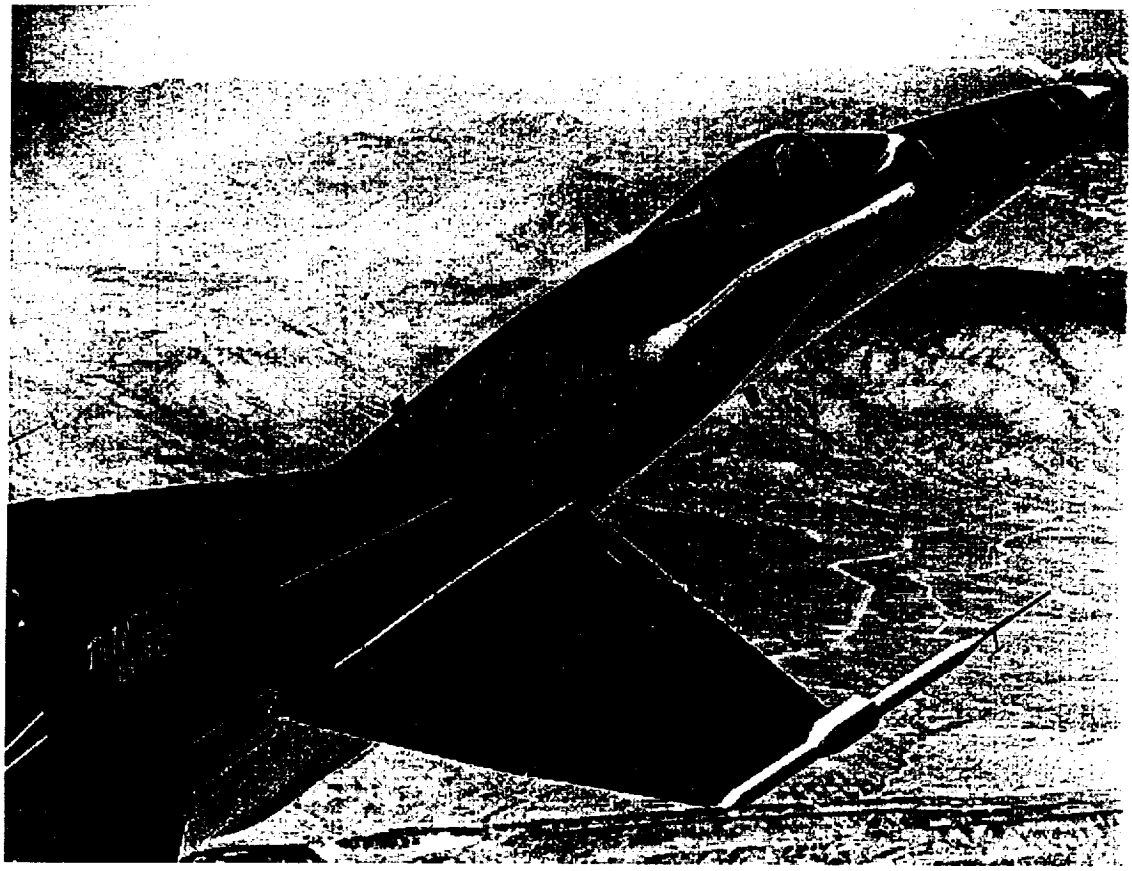

Fig. 1. Vortices are formed by the separated flow from the forebody and wings.

The development of fighter aircraft over the past several decades has culminated in the current generation of fighter aircraft, of which the F/A-18 is a typical example. The F/A-18 has a center of gravity well aft of the nose, along with wing leading edge extensions (LEX). Therefore, if yawing moment is required to maintain control of the aircraft, developing a method that takes advantage of the vortical flow field about the aircraft and the available long moment arm, from the nose to the aircraft center of gravity, would be desirable. One such method is pneumatic forebody flow control. This method uses engine

bleed air to change the flow field characteristics over the forebody of the aircraft to generate side force and yawing moment.

A form of pneumatic forebody flow control is forebody tangential slot blowing (Fig. 2). In this method, a slot is located in the nose of a fighter aircraft. Air is ejected through this slot tangential to the surface. The sheet of air remains attached to the surface through the Coanda effect, and eventually separates from the surface. The sheet of air alters the flow field and the vortices formed over the forebody, creating a side force and yawing moment. This side force and yawing moment can be used to provide directional control of the aircraft in high-angle-of-attack flight.

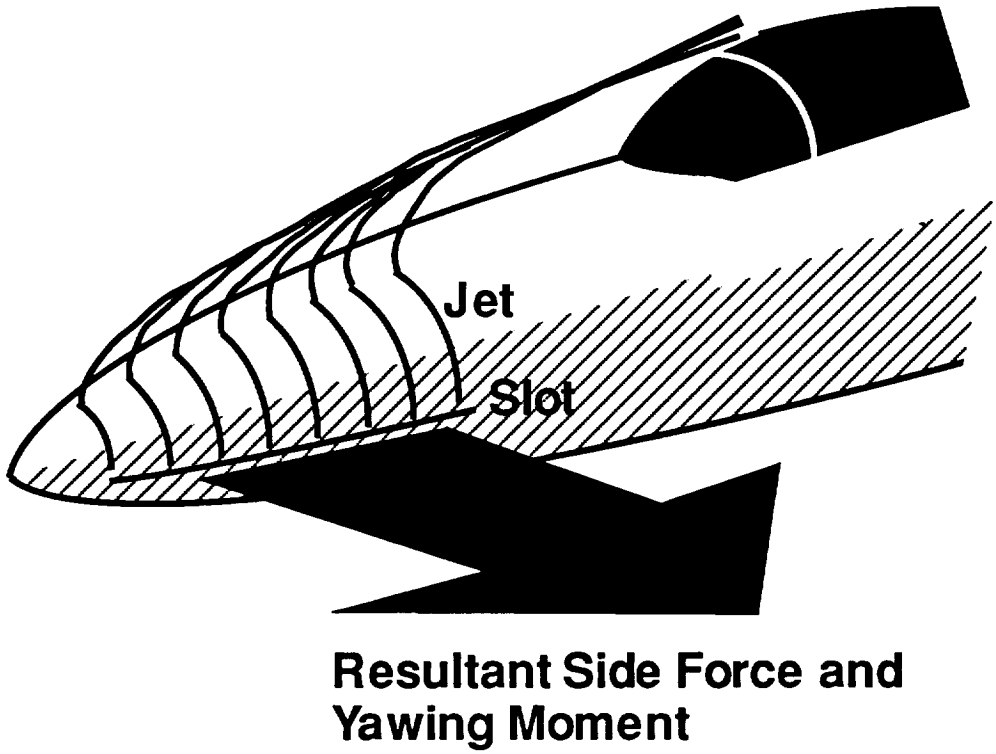

Fig. 2. Schematic of forebody tangential slot blowing.

Analysis of the tangential slot blowing concept has been performed using sub-scale water tunnel,[5,6] sub-scale wind tunnel,[7] and full-scale wind tunnel[8,9] tests on the HARV. The sub-scale water tunnel tests[5,6] have shown the effect of blowing on the vortex development over the forebody and leading edge extension (LEX) of the HARV. Qualitative force and moment data were also obtained which indicate the relative effectiveness of the system. The sub-scale[7] and full-scale[8,9] wind tunnel tests provided force and moment data, as well as surface pressure measurements. However, only limited flow visualization data was obtained; subsequently, the effect of blowing on the flow field was not well understood from the wind tunnel tests.

Therefore, analysis of tangential slot blowing is performed using computational fluid dynamics. Using CFD, a complete picture of the flow field is obtained and a thorough understanding of blowing on the vortex development can be determined. Furthermore, CFD is used to extend the experimental data, obtained at low Mach numbers, to flight Mach numbers of the HARV. In this manner, the effectiveness of forebody tangential slot blowing may be analyzed.

The next section presents the numerical method used to solve the governing equations and the grid systems used to model the HARV. Solutions are then compared with available experimental data and analyzed. Finally, conclusions are drawn about the accuracy of the numerical method and the effectiveness of forebody tangential slot blowing as a means of generating forces and moments for use in controlling an aircraft flying at high angle of attack.

Numerical Method

At large angles of attack, flow around an aircraft is characterized by large regions of three-dimensional separated flows and concentrated vortices above the aircraft. As a result, the Reynolds-averaged, thin-layer Navier-Stokes equations are solved to obtain the relevant flow features. These equations are solved numerically using the F3D[10] code. F3D is characterized as a two-factor, implicit, finite-difference algorithm using an approximate-factored, partially flux-split scheme. The F3D code has proven to be accurate and reliable in solving high-angle-of-attack problems such as the steady flow field about bodies of revolution[11] and the F-18 forebody,[12] and unsteady flow fields about the full F-18 configuration.[4] A full description of the flow solver may be found in Refs. 4, 10, and 11.

Closure of the Navier-Stokes equations is obtained using an algebraic eddy-viscosity turbulence model. In the present work, the Baldwin-Lomax algebraic model,[13] is used throughout the flow field except the forebody, the boundary layer diverter, and the region between the wing flap and the fuselage. In the forebody, the Baldwin-Lomax model with modifications for high alpha flows due to Degani and Schiff[14] is used. In the boundary layer diverter and in the region between the wing flap and the fuselage, a simplified model using only the inner-layer equation from the Baldwin-Lomax model is used. Since only the gross effects of the flow in these regions are desired, the use of such a turbulence model is adequate.[4] The Baldwin-Lomax model is used in the jet region in the present computations. In order to increase the turbulent mixing of the jet with the surrounding freestream, the Klebanoff intermittency factor is removed from the model in the jet region.

Grids and Boundary Conditions

Two types of grid systems are used to model the HARV geometry. A patched grid system is used to model the isolated forebody in the slot optimization part of the study. This grid system did not model the slot geometry per se, but rather used an actuator plane to introduce the jet conditions into the flow. An overset grid system is used to model the slot geometry in the isolated forebody grid used in the computation at wind tunnel test conditions and at the flight freestream Mach numbers. The full aircraft grid system uses the overset method. The patched grid system is initially easier to implement. However, the overset grid system is more flexible, allowing for a more geometrically accurate model. Both grid systems are described in the following sections.

Patched Grid System

The patched grid used to model the HARV isolated forebody in the slot optimization computations defines the nose and LEX of the HARV (Fig. 3), with the tip of the nose located at $x = 5.1$ ft. in Cartesian space, and the back plane of the grid located at $x = 34.25$ ft. This corresponds to fuselage station (F.S.) 60.5 for the nose and F.S. 411 for the back plane. The dimensions are equivalent to that found on the aircraft. The nose begins at F.S. 60.5 to be consistent with the aircraft blueprints.

The grid has a total of 518,000 grid points. In the section extending from the nose to the beginning of the LEX, there are 35 axial points, 101 circumferential points that describe the forebody barrel, and 50 radial points from the surface to the outer boundary, which is located approximately eight body diameters away from the surface. The section that contains the LEX has 36 axial points, 165 circumferential points, and 50 radial points.

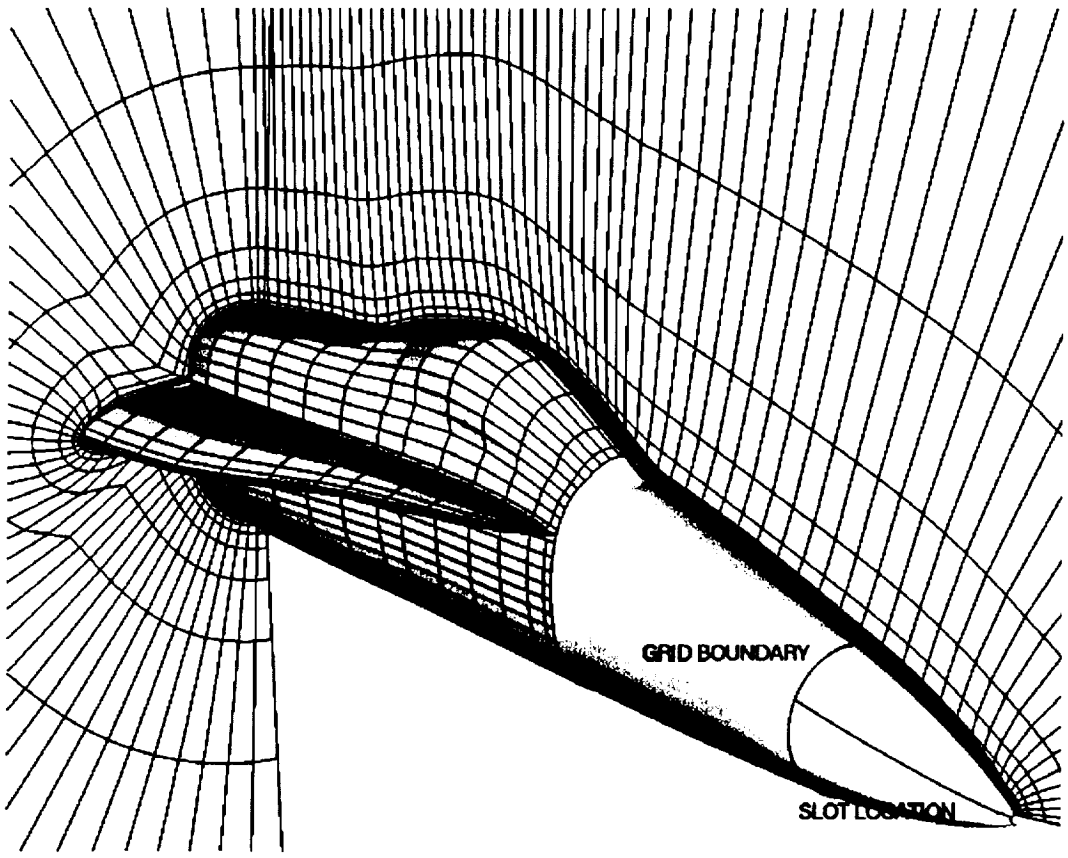

Fig. 3. Patched grid system modeling F/A-18 isolated forebody. For clarity, not all grid lines are shown.

The grid system is divided into 12 patched grids, with point-to-point matching between zones. The number of grids is dictated in part by the computer memory requirements and in part by the modeling requirements of the slot. Boundary conditions are passed between grids by direct injection where there is a zonal overlap, and interpolation where no overlap exists.

Freestream conditions are maintained at the outer boundaries. A zero-axial-gradient extrapolation is used at the outflow plane. A no-slip condition is applied at the body surface. The grid extends completely around the body circumferentially since the flow field is asymmetric due to the blowing or the presence of sideslip.

To model the slot, an actuator plane is used (Fig. 4). The grids are defined such that the slot lies along the boundary between two grid zones (Fig. 3). The actuator plane is part of the windward boundary of the upper grid (Fig. 3). There is no overlap between the two zones. The boundary values for the lower grid are obtained by zeroth-order extrapolation using the interior points of the grid for both no-blowing and blowing cases. For the no-blowing case, no new boundary conditions are introduced at the actuator plane, and the flow variables at the upper grid boundary are obtained by interpolation using the values at the grid points on either side (Fig. 4a).

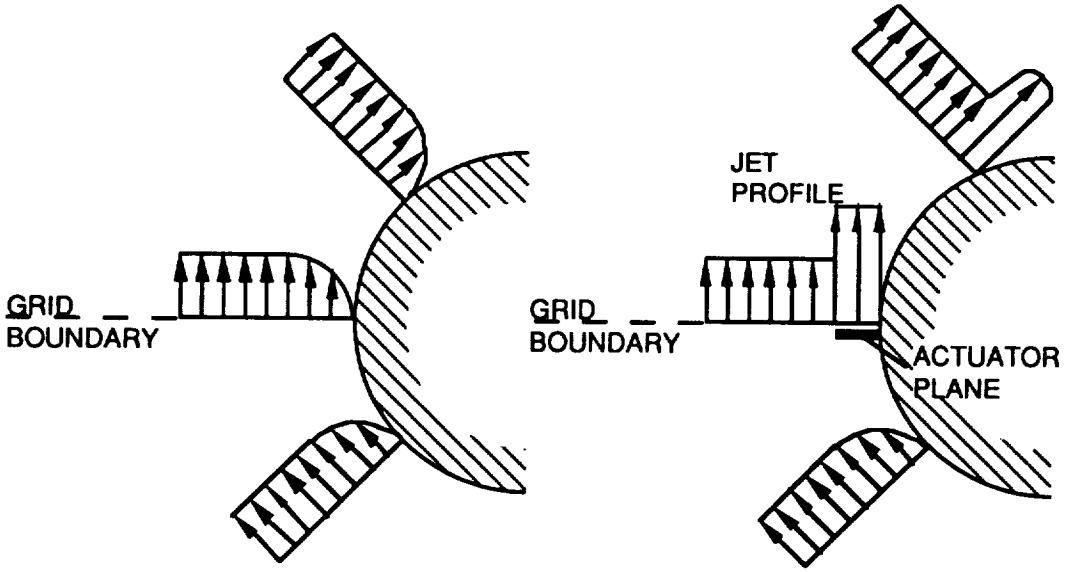

a) no blowing

b) with blowing

Fig. 4. Schematic of actuator plane implementation in the patched grid system.

For the blowing case, the flow variables in the actuator plane are overwritten with the jet conditions (Fig. 4b). It is assumed that the jet total pressure, P_t, is known and is equal to 1.415 times the ambient pressure, P_a. The total pressure is used to determine the jet exit Mach number, M_j, by assuming that the exit pressure, P_j, is equal to freestream, and the flow is isentropic. For the chosen pressure ratio, $M_j = 0.72$. Upon setting the jet static exit temperature, T_j, to the freestream value, the density and energy of the jet are determined. Note that setting the jet exit pressure to freestream introduces a slight error into the computations, since the local pressure at the jet exit is not precisely that of the freestream, but this error is slight and the flow recovers quickly from the discontinuity. These slot boundary conditions are identical to those used in the previous computations by Tavella et al.[15] and Murman et al.[16] All the slot geometries investigated in this study have

the same P_t and M_j. As a result, the jet mass flux and momentum coefficients are dependent only upon the area of the slot.

Overset Grid System

The remainder of the study is performed using computational grids based on the overset scheme.[17] In this method, two adjacent grids need only to overlap; no other restrictions are placed on the abutting surfaces. By requiring that grids overlap instead of match faces, grid generation is simplified. Furthermore, additional grids, such as the slot grids in the present problem, may be added to existing grids without large-scale changes to the existing grid system. Further improvements to this method were made[3] such that grids can either touch faces or overlap. This adds additional flexibility to the scheme, especially when gridding intersecting components of the aircraft.

The individual grids are generated using a hyperbolic procedure.[18] This method generates orthogonal or near-orthogonal grids, and allows for user-specified spacing near the surface. It has the further advantage of being fairly inexpensive to use in terms of computer time and memory. The one disadvantage is the inability to specify an exact outer boundary location. However, this limitation does not have a large affect on the present work since face-to-face matching is not required in the Chimera scheme.

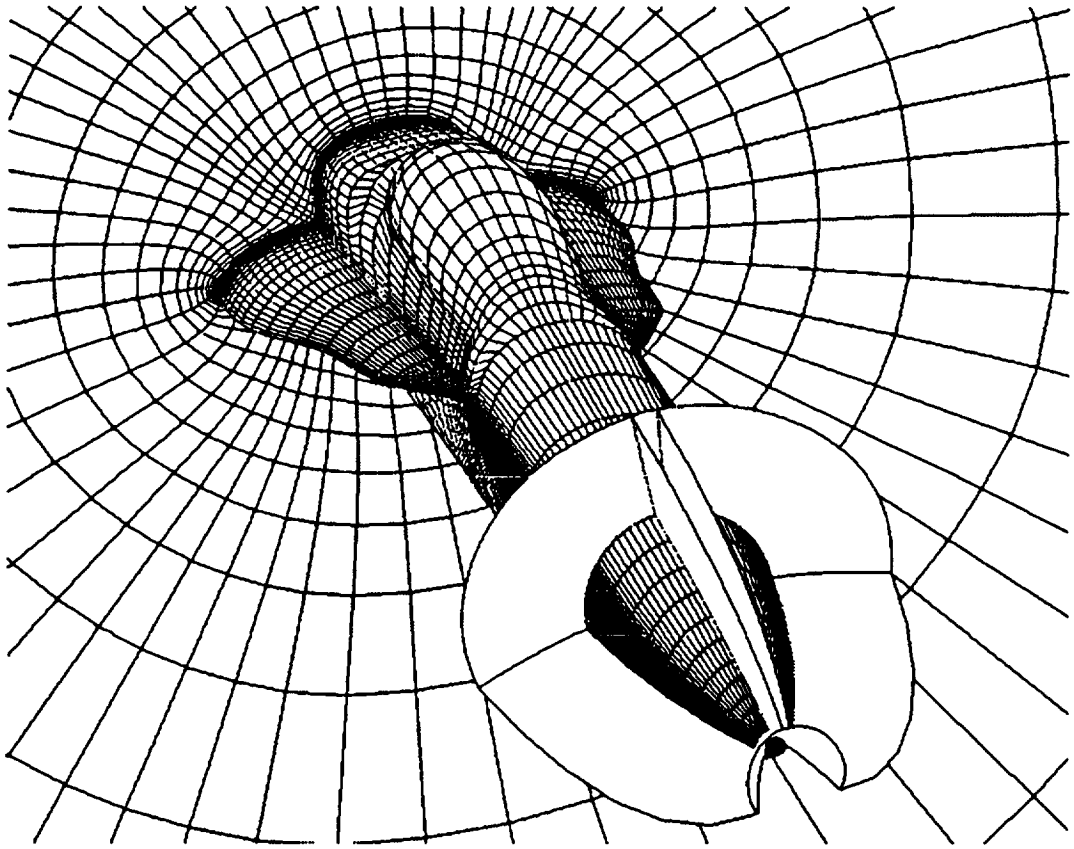

Fig. 5. Grids modeling experimental slot geometry in overset grid system.

The overset isolated forebody grid system (Fig. 5) consists of six grids. Two grids define the slot geometry, two define the fuselage forebody, and two define the farfield region. The forebody grids consists of 39 axial, 121 circumferential, and 49 normal points (not including the inviscid outer grid). It is expected that the present grid will resolve the crossflow separation lines on the nose more accurately than the patched grid system, by virtue of increased circumferential grid density in this region. Computations[16] implementing the overset or Chimera[17] scheme to model the slot geometry showed the slot geometry has a local effect on the flow near the slot for no-blowing solutions. The flow solution with blowing was similar to the solution obtained using the actuator plane method.

The slot geometry used in the full-scale wind tunnel experiment (Fig. 6) is modeled using two grids (Fig. 5). Slots are included on both sides of the body to match the experimental configuration, although blowing occurs only from the slot located on the pilot left. The slot grids extend from the slot location to the leeward plane of symmetry and from the surface into the farfield. This simplified the implementation of an algebraic turbulence model in the slot region. To check the effect of the slot grids on solution accuracy, no-blowing solutions are obtained with the slot grids in place and compared with no-blowing experimental data. These results are discussed in a later section.

The full HARV grid geometry is shown in Fig. 7. It is comprised of twenty grids containing a total of 1.8 million grid points. The wing leading-edge flaps are deflected 33° nose down, the trailing-edge flaps are not deflected, and the horizontal tails are deflected 7° nose down. The deflection angles of these control surfaces correspond to the trim flight condition of the HARV at $\alpha = 30°$. The major features of the aircraft are well represented. However, several simplifications to the geometry are made to facilitate modeling. The engine inlets are faired over, with no flow through the fairing. The boundary layer diverter grid is highly simplified. An analogous 10-grid model has been used in previous full-body, zero-sideslip computations, which gave good results when compared with flight-test data.[4]

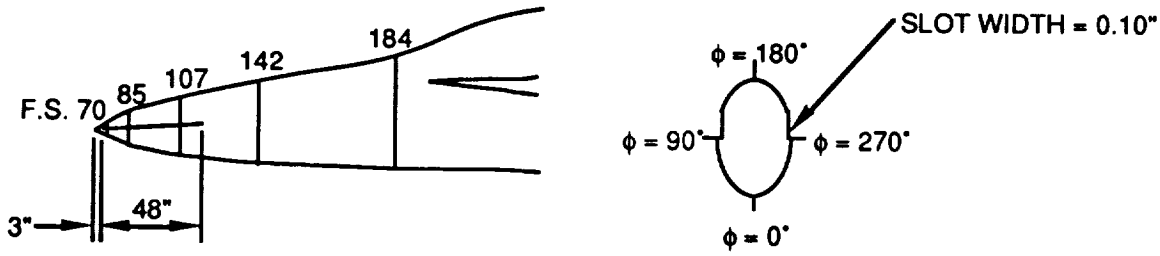

a) Side view of forebody showing slot and pressure ring locations.

b) Cross-section through slot region.

Fig. 6. Slot geometry used in full-scale wind tunnel tests.

The outer boundaries of the grid system lie 5.6 mean aerodynamic chord (MAC) lengths in front of the body, 8.7 MAC lengths above and below the body, and 9.5 MAC lengths behind the body. A sting is used behind the body and extends to the exit plane. At the body surface, no-slip and solid-wall boundary conditions are applied. Freestream conditions are imposed at the outer boundaries, and a zero-gradient extrapolation boundary condition is used at the outflow boundary. At grid boundaries that overlap adjacent grids,

boundary conditions are obtained using the Chimera and Pegasus[17] approach. For the slot grids, an overlap of approximately one grid point is used on all outer boundaries except the surface.

Previous computations[15,16] modeled the jet by specifying the Mach number, density, and exit pressure of the jet. Both the density and exit pressure were set to freestream values. The current isolated forebody computation utilize boundary conditions that are more physically realistic. The jet exit Mach number and the jet mass flow rate are obtained by matching the full-scale experimental conditions. For subsonic jet exit Mach numbers, the jet exit pressure is assumed to be the local pressure value at a point just above the slot, in the direction normal to the body surface. This exit pressure is updated at each iteration step. The density of the jet is computed from the known mass flow rate, jet exit Mach number, and the measured plenum temperature.

To extrapolate wind tunnel data to flight conditions, the jet exit Mach number and the jet mass flow rate are obtained by matching the jet mass flow ratio (MFR) with the full-scale experimental data. The mass flow ratio is defined as the ratio of the jet mass flow rate and the reference mass flow rate, which is based on the freestream density, velocity, and wing area. If the jet exit Mach number is less than sonic, the jet total pressure and total temperature are input into the flow solver. The exit pressure is obtained by extrapolating the pressure from the local external flow pressure at the jet exit and the jet exit Mach number is obtained using the isentropic relations. For sonic flow, the jet is assumed to choke at the exit and the jet exit pressure is obtained from isentropic relations using the jet total pressure and temperature inputs. In either case, in order to obtain the desired MFR value, the total pressure of the jet is increased, thereby increasing the jet density, until the desired jet mass flow rate is obtained.

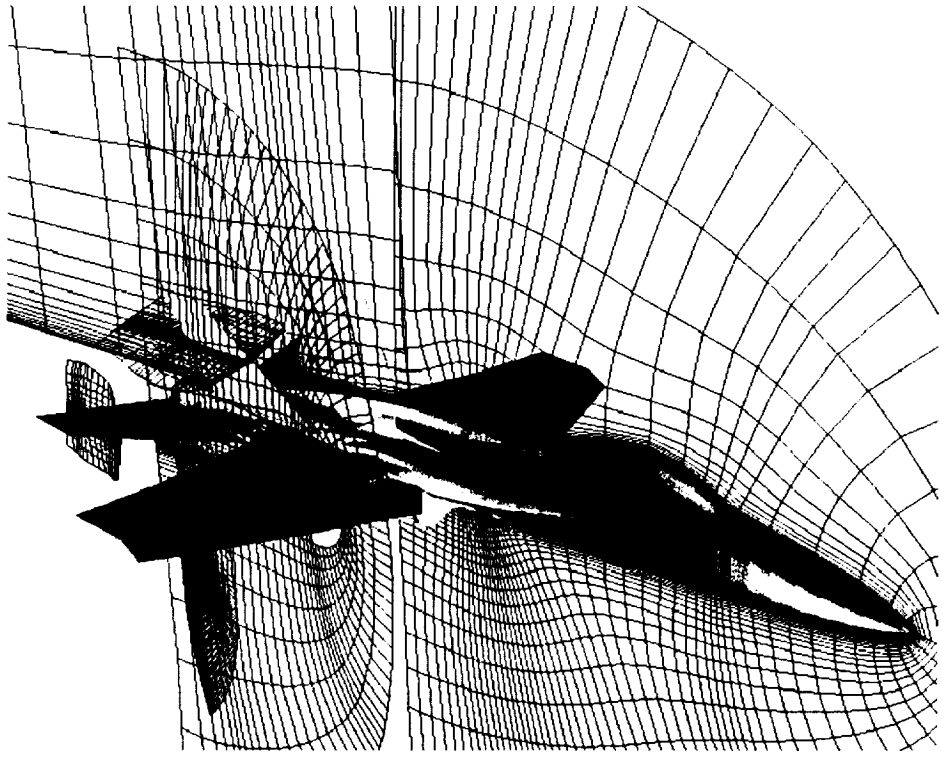

Fig. 7. Overset grid system used to model full F/A-18 geometry.

Results

The computational analysis proceeded in four phases. The initial solutions were obtained using a patched grid system to model the HARV isolated forebody. Patched grids were used to reduce the amount of memory required on the Cray 2 supercomputer and to facilitate modeling of the jet. The jet was modeled using the actuator plane concept. The initial study was intended to develop a baseline slot geometry for use in full-scale wind tunnel tests. Efficiency of the slot geometry was defined as the amount of side force and yawing moment developed per unit blowing coefficient. Different active slot geometries were analyzed, as well as the efficiency of the blowing system in a sideslip condition.

Once experimental data became available, a solution was obtained at wind tunnel test conditions to determine the accuracy of the numerical method. For this case, an overset grid system was used to model the HARV isolated forebody. The overset grid system was used because it allowed for the modeling of the backward-facing step of the slot geometry, which was not practical under the patch grid system used in the first part of the analysis. The jet conditions were introduced as boundary conditions in the grid used to model the slot geometry. The accuracy of the method was measured by comparing computed and measured surface pressure coefficient data.

The use of the overset grid method to model the isolated forebody in the second phase of the analysis was a natural precursor to the third phase, which was computing the flow field about the full HARV aircraft geometry with tangential slot blowing. The solutions for this case were obtained at typical flight conditions in order to extend the analysis from wind tunnel to flight conditions. In order to compare with available experimental data, the jet conditions were set such that the mass flow ratio (MFR) of the computations matched existing experimental mass flow ratios. Thus, the computational results would also serve as a check of the correlation parameter developed by the wind tunnel experimentalists. A time-accurate solution was also obtained to determine the effect of blowing on the aerodynamic loads on the vertical tails, since blowing has an effect on the flow field characteristics, especially the burst point of the LEX vortices.

The final phase used the isolated forebody grid system to determine the effect of freestream Mach number and mass flow ratio on blowing. Since a matrix of solutions was desired to evaluate trends, the smaller grid system of the isolated forebody, as compared with the aircraft grid system, was used. This reduced the amount of computer time required per solution. The effect of freestream Mach number is important since the HARV, and the F/A-18, was capable of entering high angle of attack flight at transonic Mach numbers.

The analysis carried out provides a good understanding of the effects of forebody tangential slot blowing on the flow field about the HARV. The results indicated that such a pneumatic flow control system was a viable means of providing the necessary control power while flying at high angle of attack. The computational results provided a detailed picture of the flow field and the effect of blowing on the flow field, which complimented the results obtained from the experiments. The results of this investigation will help aircraft designers develop more maneuverable and safer aircraft.

Slot Efficiency Study

The flow about the forebody of the HARV is computed using the flow solver described in the Numerical Methods section. The grid system used in this part of the study is shown in Fig. 3. For this part of the study, patched grids and an actuator plane are used to model the isolated forebody geometry and the jet (Fig. 4). To accommodate the actuator plane, the grid is divided into zones such that the slot lies along the boundary between two zones.

Due to computer memory limitations, the grid is further divided into a total of 12 zones. Steady-state solutions are obtained using a Cray Y-MP or a Cray-2 supercomputer. Typical solutions required 4MW of memory and about 40 Cray-2 CPU hours for convergence.

The flow conditions in these cases are $M_\infty = 0.20$, $\alpha = 30°$, and $Re_{\bar{c}} = 11.52 \times 10^6$. Cases are obtained for flow with no sideslip, $\beta = 0°$, and with a sideslip angle of $\beta = -10°$, to determine how sideslip influences the control forces generated by tangential slot blowing. Several slot geometries are investigated at zero sideslip to determine the effects of slot location and slot length on the effectiveness of the control system. The efficiency of the system, η_b, is measured by the amount of side force and yawing moment that is obtained per unit momentum blowing coefficient. The momentum blowing coefficient, C_μ, is defined as

$$C_\mu = \frac{\rho_j A_j V_j^2}{q_\infty S} \tag{1}$$

Slot Configurations

The slot configurations investigated (Fig. 8) differ in the length of the slot and the location of the slot on the forebody. All of the slots used in this study have a nominal width, h_l, of 0.156 in., and all slots have the same pressure ratio, $P_t/P_j = 1.412$,, and jet exit Mach number, M_j. =0.72.

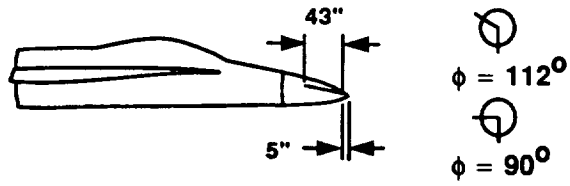

a) 43 in. slot configuration

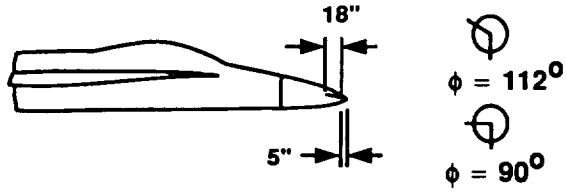

b) 18 in. slot configuration

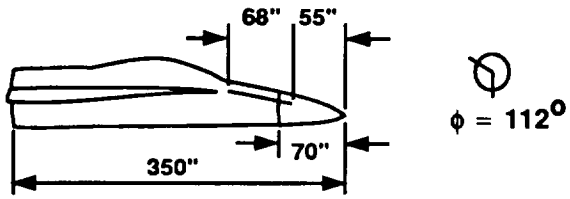

c) 68 in. slot configuration

Fig. 8. Slot configurations considered in optimization part of study.

It is well recognized, from both experimental and computational studies, that small disturbances placed close to the nose of a body of revolution at large incidence produce large asymmetries in the flow.[19,20] Using this principle as a guide, the initial slot design was developed. This configuration has a 43 in. slot located 5 in. from the nose (Fig. 8a). For this slot geometry, $C_\mu = 0.0027$. The length of the slot is dictated in part by the desire to place the entire length of the slot within the radome of the test aircraft. Two circumferential locations are studied, with $\phi = 112°$ and $\phi = 90°$.

The second slot configuration is a shortened version of the previous slot. The length of the slot is reduced from 43 in. to 18 in., while the leading edge of the slot remains located 5 in. from the nose of the aircraft (Fig. 8b). For this slot, $C_\mu = 0.0013$. Again, two circumferential locations are studied, with $\phi = 112°$ and $\phi = 90°$. Shortening the slot has the benefit of reducing the blowing coefficient of the configuration. However, it has been found for bodies of revolution at high incidence that varying the size of the perturbation at a fixed location on the body has a large effect on the side force obtained.[20,21] Thus, it is necessary for the present configuration to determine how shortening the slot will affect the character of the flow field and the efficiency of the system.

These two configurations are compared against a slot configuration that is 68 in. long, with its leading edge located 55 in. from the nose (Fig. 8c). This slot is set at a circumferential angle of $\phi = 112°$, measured from the windward plane of symmetry. The blowing coefficient for this slot is $C_\mu = 0.005$. Computed solutions obtained for this configuration were originally reported in Ref. 15.

Forces and Moments at Zero Sideslip

One of the thrusts of this study is to determine an efficient slot configuration to be used for further study in wind tunnel experiments. Efficiency is defined as the amount of side force and yawing moment obtained per unit momentum blowing coefficient. Forces and moments are obtained by integrating the surface pressure distribution only. Positive side force is defined such that it moves the body in the positive direction of the y-axis. Positive yawing moment turns the nose of the body in a clockwise direction (Fig. 9).

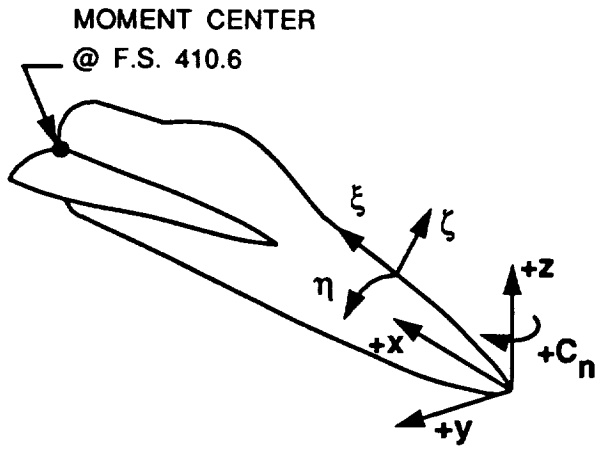

Fig. 9. Coordinate system and moment center used in optimization part of study.

For the case of zero sideslip, the computed side-force coefficient for each configuration is plotted as a function of its momentum coefficient in Fig. 10. As the length of the slot is reduced, C_μ is reduced, but the amount of side force does not drop significantly. Even though the 68 in. slot generates the largest incremental change in C_Y, it is the least efficient of the slot configurations studied, with $\eta_b = 13.0$. The 18 in. slot proves to be the most efficient, with $\eta_b = 38.5$. This is due to the shorter slots being located closer to the nose of the aircraft. A large gain in efficiency is obtained by using the 18 in. slot, since there is only a small loss in side force for a reduction of C_μ by a factor of two, when compared with the 43 in. slot. From these results, a short slot near the nose of the aircraft provides the most lateral control force for the smallest amount of C_μ.

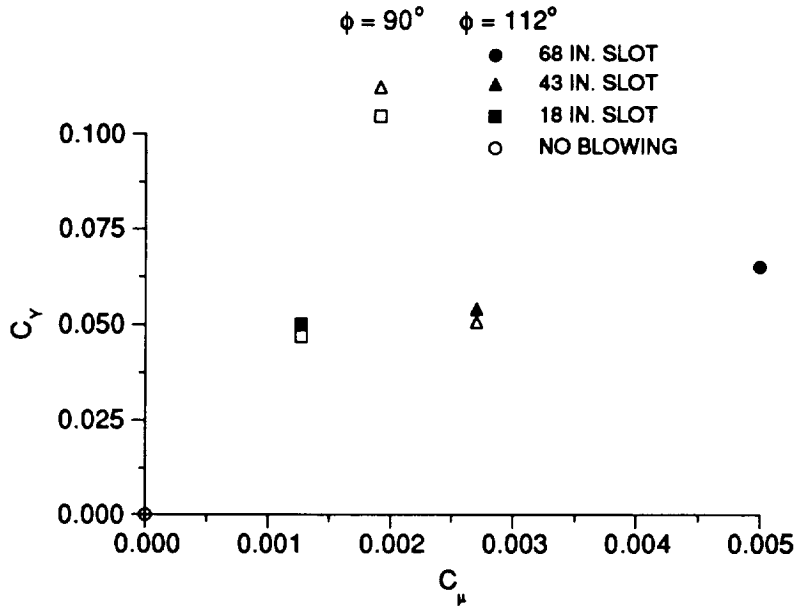

Fig. 10. Computed side force coefficient plotted against momentum coefficient. $M_\infty = 0.20$, $\alpha = 30°$, $Re_{\bar{c}} = 11.52 \times 10^6$.

For the two short slots, locating the slot further towards the windward side ($\phi = 90°$) reduces the side force by about 6%, in comparison with the same length slot located at $\phi = 112°$ (Fig. 10). Analogous trends may be seen for the computed yawing-moment coefficient (Fig. 11). Note that the moments are taken about the back plane of the computational grid, which is at F.S. 410.6 (Fig. 9).

Flow Characteristics at Zero Sideslip

One method of understanding the changes in the flow field due to the slot blowing is by studying the surface flow patterns, shown in Fig. 12. The surface flow pattern is obtained by integrating the velocity vectors located one grid point above the surface.

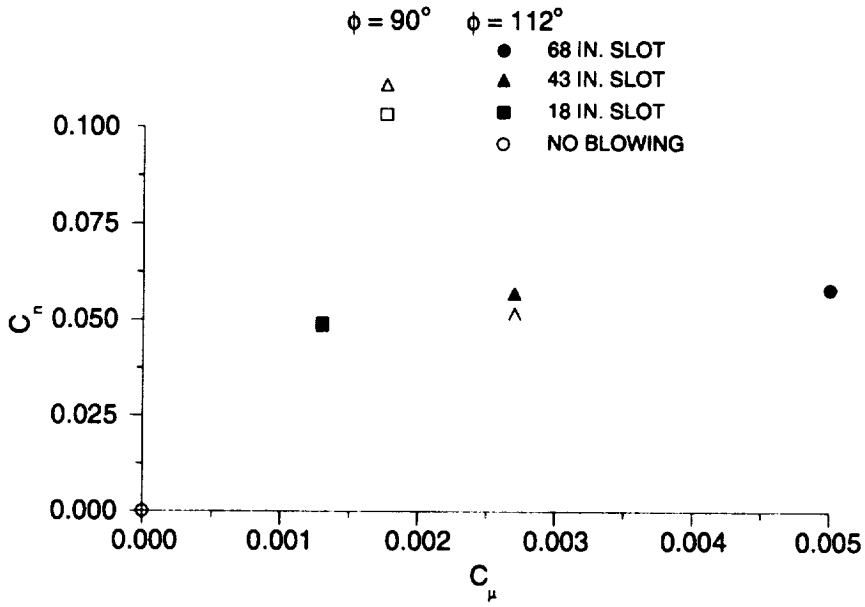

Fig. 11. Computed yawing moment coefficient plotted against momentum coefficient. $M_\infty = 0.20$, $\alpha = 30°$, $Re_{\bar{c}} = 11.52 \times 10^6$.

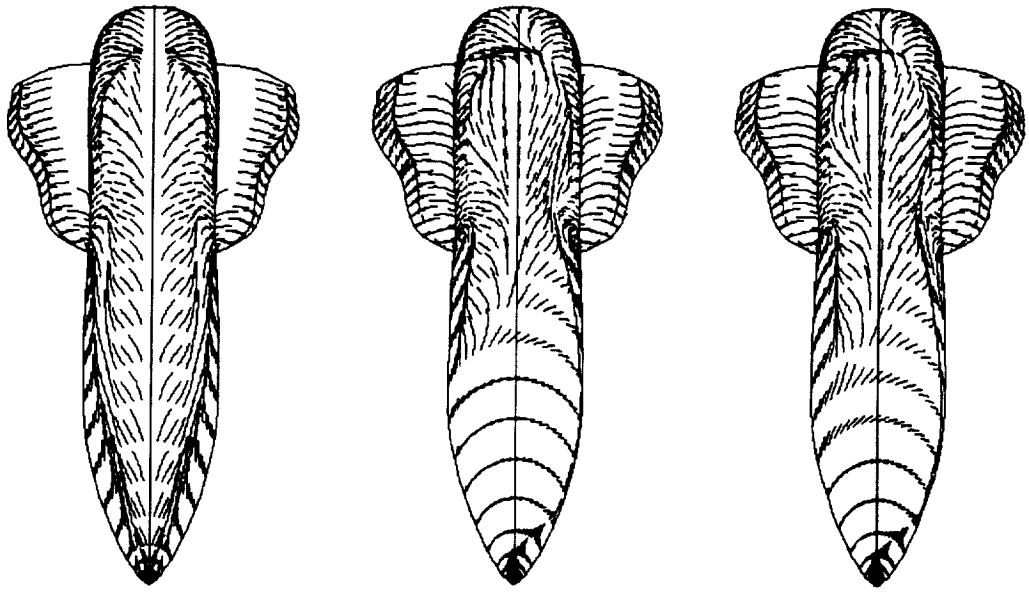

a) no blowing **b)** blowing, 43 in. slot **c)** blowing, 18 in. slot

Fig. 12. Computed surface flow pattern. $M_\infty = 0.20$, $\alpha = 30°$, $Re_{\bar{c}} = 11.52 \times 10^6$.

The surface flow pattern obtained from the no-blowing solution (Fig. 12a) shows good agreement with surface flow patterns obtained from flight experiments.[12] The primary and secondary crossflow separation lines on the forebody are clearly seen, as well as the secondary separation lines on the leading-edge extension (LEX).

Comparing the baseline flow pattern with that obtained from the solution using the 43 in. slot (Fig. 12b) shows the effect of slot blowing on the flow field. In the slot region, the jet remains attached to the surface well past the leeward plane of symmetry so that only one primary separation line appears, located on the non-blowing side. At this line, the jet separates from the surface. Aft of the slot, on the blowing side, a separation line forms at about the same circumferential location as the primary separation line of the no-blowing case. Shortening the slot from 43 in. to 18 in. changes the surface flow pattern slightly (Fig. 12c). The jet separation line on the non-blowing side is located further towards the leeward plane of symmetry. The crossflow separation line that forms aft of the slot on the blowing side is located further leeward as well. Since the slot is shorter, the flow begins to turn downstream much sooner in the 18 in. slot solution (Fig. 12c) than in the 43 in. slot solution (Fig. 12b). The flow patterns in the aft portion of the body show some slight changes. The LEX secondary separation lines move slightly inboard in the solutions with blowing (Fig. 12b,c). The flow is also asymmetric in the region of the canopy. These changes in the flow field between the 43 in. and 18 in. slot solutions account in part for the differences in the side force and yawing moment obtained for these two blowing cases.

Helicity density contours[22] help visualize the changes in the off-body flow field due to blowing (Fig. 13). In this figure, the lines represent constant values of helicity density, with the largest values located in the core of the vortices. Solid lines represent clockwise rotation of the flow, while dashed lines represent counterclockwise rotation, when viewed from the front of the aircraft. There are observable differences in the relative strength of the LEX primary vortices between the no-blowing (Fig. 13a) and blowing solutions (Fig. 13b,c). The no-blowing solution has a stronger set of LEX primary vortices than do the blowing solutions. Since the primary LEX vortices are initially stronger in the blowing cases, the secondary vortices are stronger as well. The LEX primary vortex on the non-blowing side is weaker than the one on the blowing side in Fig. 13b and Fig. 13c. The interaction between the forebody vortex structure due to the jet and the flow field over the LEX causes the asymmetry seen in the blowing solutions. Furthermore, the helicity contours indicate a vortical structure close to the surface in the area of the canopy for the slot blowing cases (Figs. 13b,c) which does not exist in the no-blowing case (Fig. 13a). This asymmetry near the canopy causes the surface pressure on the blowing side to be lower than the pressure on the non-blowing side.

A change in the circumferential location of the slot from $\phi = 112^\circ$ to $\phi = 90^\circ$ alters the forebody vortical structures and the structure over the canopy (Fig. 14). For the 18 in. slots, the primary forebody vortex creates regions of vorticity that separates from the body along the axial direction. However, for the slot at $\phi = 90^\circ$, there is a region of clockwise helicity on the non-blowing side of the canopy area (Fig. 14b) which is not apparent in the solution with the slot at $\phi = 112^\circ$ (Fig. 13c). The LEX vortices do not exhibit any noticeable differences between the two solutions. The differences near the nose and over the canopy and LEX region accounts for the difference in side force and yawing moment between these two cases.

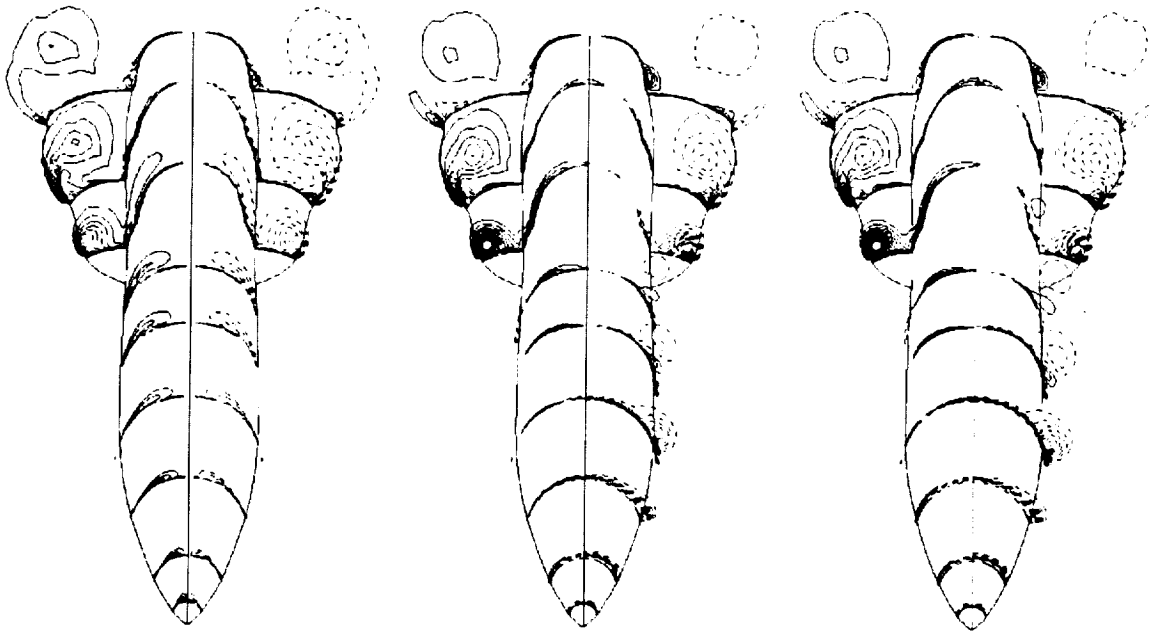

a) no blowing b) blowing, 43 in. slot c) blowing, 18 in. slot

Fig. 13. Computed surface flow pattern. $M_\infty = 0.20$, $\alpha = 30°$, $Re_{\bar{c}} = 11.52 \times 10^6$.

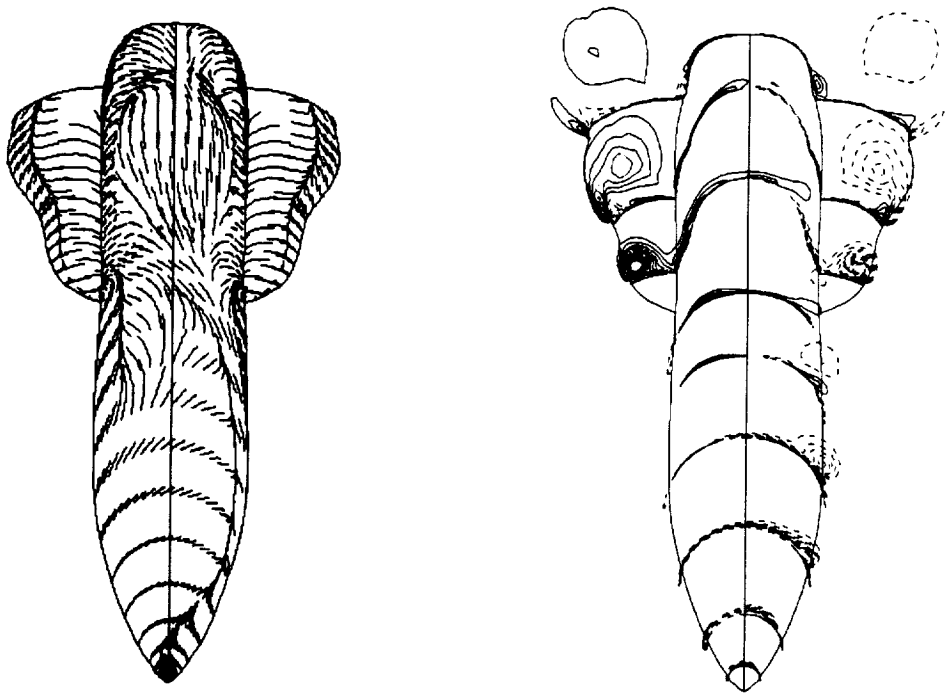

a) surface flow pattern b) helicity density contours

Fig. 14. Visualization of solution with 18 in. slot at $\phi = 90°$.
$M_\infty = 0.20$, $\alpha = 30°$, $Re_{\bar{c}} = 11.52 \times 10^6$.

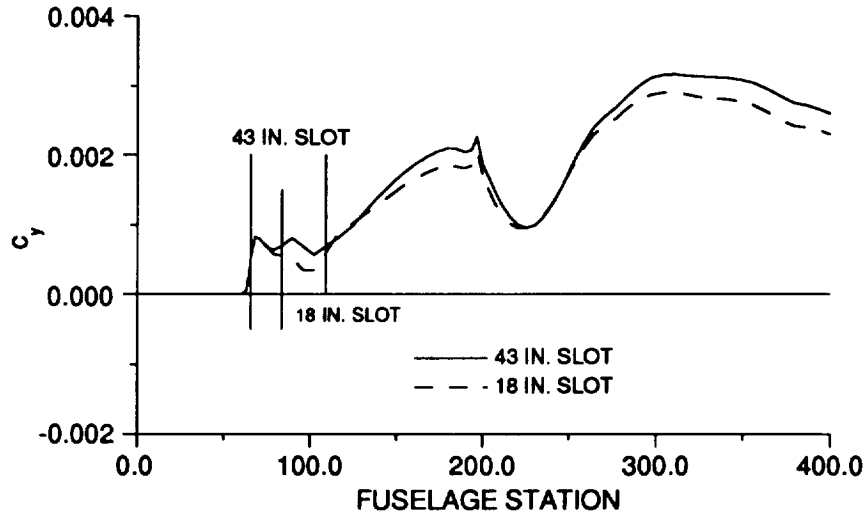

a) Effect of slot length at $\phi = 112°$

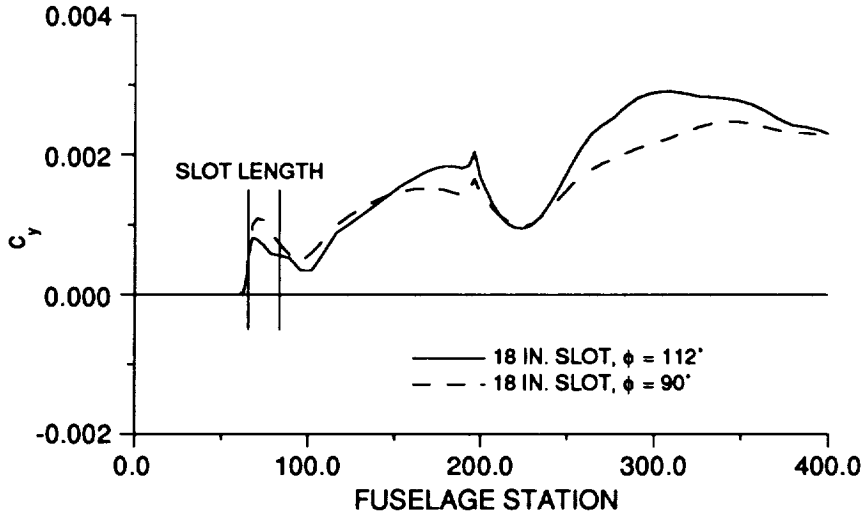

b) Effect of slot circumferential location, 18 in. slot.

Fig. 15. Comparison of side force distribution along the forebody.
$M_\infty = 0.20$, $\alpha = 30°$, $Re_{\bar{c}} = 11.52 \times 10^6$.

The change in the local surface pressure in the LEX region helps explain how tangential slot blowing generates side force. In the slot region, a low pressure region is caused by the jet remaining attached to the surface, whereas on the non-blowing side, the flow has separated and a higher pressure region exists. Changes in the flow field near the nose due to blowing cause changes in surface pressure, and thus the local side-force distribution, along the entire body (Fig. 15a). For cases with zero sideslip, there is a positive side force

(force acting in the +y direction) along the entire length of the body. The side force is due mainly to the interaction of the new flow field caused by the jet on the nose with the remainder of the flow field. Note that a circumferential change in the slot location from $\phi = 112°$ to $\phi = 90°$ (Fig. 15b) for the 18 in. slot increases the side force in the slot region. However, the side force along the remainder of the body is reduced. Thus, the slot located at $\phi = 90°$ generates slightly less total side force than the slot located at $\phi = 112°$. Results computed using the 43 in. slot are similar. It appears that the mechanism in slot blowing which generates the side force and yawing moment is the interaction of the separated jet vortical structure with the remainder of the flow field.

Flow Characteristics with Sideslip

The effects of sideslip were studied by obtaining solutions using the 43 in. slot located at $\phi = 112°$ and a sideslip of $\beta = -10°$ (Fig. 16), with all other parameters the same as in the no-sideslip case. Blowing from slots on the pilot-right and pilot-left side of the fuselage are investigated. Since the forebody blowing concept apparently generates lateral control by keeping the jet attached to the surface and displacing the forebody vortices, the effectiveness of the concept may be degraded when the aircraft is flying at an angle of sideslip. In this case, the separation lines and vortices are displaced from symmetry due to the oncoming wind. This behavior is clearly shown in the no-blowing surface-flow pattern with $\beta = -10°$ (Fig. 17a). On the forebody, the windward primary separation line is rotated almost to the leeward centerline, with the separation line extending over the canopy. The leeward separation line rotates in similar fashion away from the wind direction. The LEX secondary crossflow separation line are also affected by the wind direction. The windward LEX primary vortex and secondary crossflow separation line are moved inboard, while the primary vortex and secondary crossflow separation line on the leeward LEX is shifted outboard.

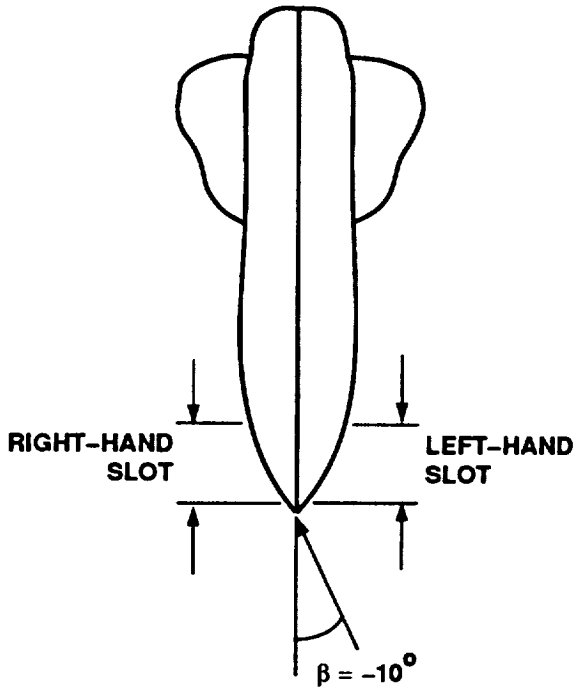

Fig. 16. Schematic of sideslip direction and slot orientation for cases with sideslip.

For the blowing system to be effective, it must generate enough side force and yawing moment to overcome the force and moment imparted on the entire aircraft due to the sideslip. However, the current study cannot predict such behavior since only the forebody is included in the computations. The contribution of the wings and empennage to the control of the aircraft, and the interaction of the new forebody flow field due to blowing with these surfaces cannot be determined from this part of the study. However, the present study does provide a good indication of the interaction of the forebody flow with the LEX flow in sideslip conditions.

The effect of blowing on the surface flow pattern for cases with sideslip is shown in Fig. 17. Blowing from a slot on the pilot right (Fig. 17b) produces a surface flow pattern similar to the no-sideslip case (Fig. 12b). In this case, the jet is moving in a direction opposite that of the local sideslip. The jet separation line is pushed well past the plane of symmetry, and although not shown in the figure, a separation line forms aft of the slot on the blowing side. No large changes are evident in the surface flow patterns on the LEX, but the flow in the canopy area is altered. The forebody primary separation line that extends over the canopy (Fig. 17a) no longer appears in the right-hand blowing case (Fig. 17b).

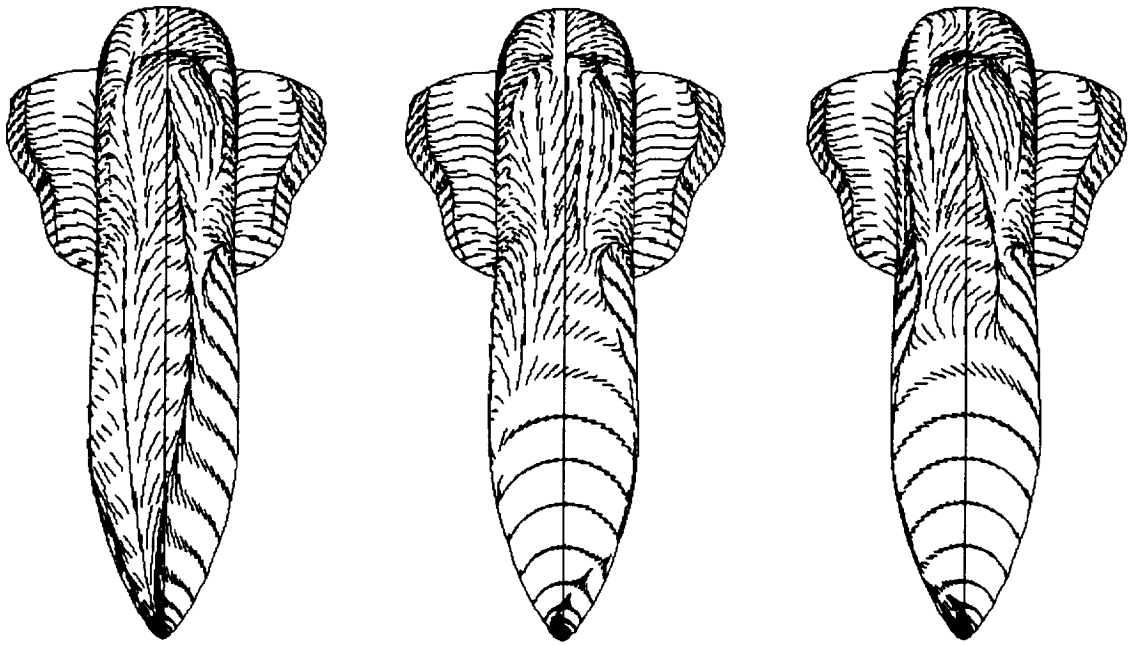

a) no blowing **b)** starboard blowing **c)** port blowing

Fig. 17. Computed surface flow pattern, cases with sideslip.
$M_\infty = 0.20$, $\alpha = 30°$, $Re_{\bar{c}} = 11.52 \times 10^6$.

Blowing from the opposite side of the fuselage (pilot's left) causes the blowing to augment the effect of the local sideslip. In this case, the jet is moving in the direction of the local sideslip. The blowing forces the jet separation line well past the symmetry plane (Fig. 17c), merging with the separation line on the non-blowing side. However, in this case, a

separation line forms aft of the slot in about the same location as the primary separation line in the non-blowing case (Fig. 17a). The jet separation line on the non-blowing side turns upward towards the leeward plane of symmetry, just as in the right-hand blowing case. Similar to the case of blowing from the right-hand side, no large changes are observed in the surface flow pattern on the LEX with blowing on the left.

Helicity density contours (Fig. 18) shows the changes in the forebody and LEX vortices due to the combined effect of sideslip and blowing. In the no-blowing case (Fig. 18a), the two primary forebody vortices are clearly seen, with the windward vortex running along the centerline of the body, over the canopy region. The windward LEX primary vortex is pushed closer to the body, while the leeward LEX primary vortex is shown to be pushed outboard from the body.

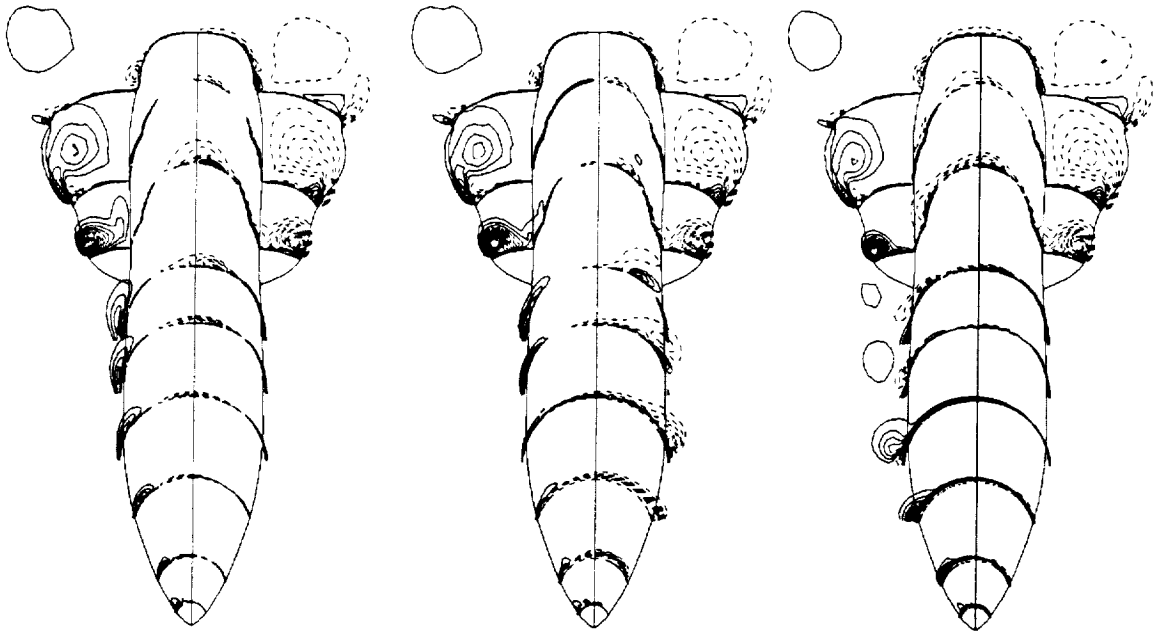

a) no blowing b) starboard blowing c) port blowing

Fig. 18. Computed helicity density contours, cases with sideslip. $M_\infty = 0.20$, $\alpha = 30°$, $Re_{\bar{c}} = 11.52 \times 10^6$.

Blowing from the right-hand side (Fig. 18b) alters the forebody flow structure in much the same way as blowing with no sideslip. However, there are changes in the LEX region. Blowing from the right-hand side appears to weaken the windward primary LEX vortex, with no change observed in the leeward one. Weakening the windward LEX primary vortex causes an increase in the pressure on the windward side. Blowing from the left-hand side has the opposite effect (Fig. 18c). In this case, the leeward LEX primary vortex is weakened and moved further outboard. This increases the pressure on the leeward side of the body. Also, blowing has the direct effect of reducing the pressure on the nose such that a net force to the left is obtained. The net result of the changes in the pressure distribution is discussed in the next section.

Forces and Moments with Sideslip

As with the no-sideslip results, blowing in flows with sideslip generates forces and moments acting in the direction of the slot. That is, blowing from the right-hand side causes positive increments in side force and yawing moment. Plotting the side-force coefficient against the sideslip angle shows this trend clearly (Fig. 19). For the case with zero sideslip, the no-blowing case will have zero side force, due to symmetry. Blowing on the right-hand side produces a positive incremental change in the side-force coefficient. The side force is directed towards the side with the slot. Because of flow symmetry, the magnitude of the incremental change in side force due to blowing will be equal for blowing from the right- and left-hand side at zero sideslip.

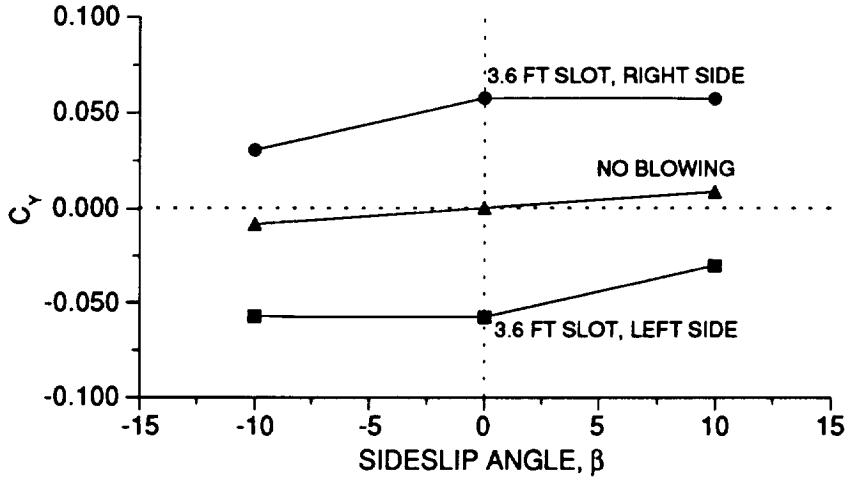

Fig. 19. Effect of sideslip angle and slot location on side force coefficient. $M_\infty = 0.20$, $\alpha = 30^\circ$, $\beta = -10^\circ$, $Re_{\bar{c}} = 11.52 \times 10^6$.

The same is not true for the cases with sideslip, since the no-blowing flow is no longer symmetrical. Blowing from the right-hand slot produces a positive incremental change in side force that is about 50% less than that obtained in the no-sideslip case. Blowing from the left-hand side causes an incremental change in the negative direction that is about equal to that obtained for the no-sideslip case. Also, it can be seen that the change in side force obtained by blowing from the right-hand side in a flow with negative sideslip is equivalent to that obtained by blowing from the left-hand side in a flow with positive sideslip. Thus, the incremental changes in side force for cases with a positive sideslip angle of $\beta = +10^\circ$ shown in Fig. 19 are obtained from the solutions with a negative sideslip angle by reflection.

The trends observed in the side-force coefficient plot (Fig. 19) are also evident in a plot of the yawing-moment coefficient versus the sideslip angle (Fig. 20). At zero sideslip angle, flow symmetry dictates that the no-blowing case produces zero yawing moment. Blowing from the right-hand side generates a positive incremental change in the yawing moment. With sideslip, the baseline no-blowing solution indicates the body undergoes a positive yawing moment. Blowing on the right-hand side generates a positive incremental change in the moment (Fig. 20) that is slightly smaller than the change observed in the no-sideslip case. Blowing on the left-hand side yields a negative incremental change that is about equal

in magnitude with that for the no-sideslip case. The moment coefficients for the positive sideslip angle, $\beta = +10°$, are again obtained by reflecting the negative sideslip solutions. Data at smaller sideslip angles are required to determine the correct slope of the curves in Fig. 20, but certain trends can be obtained from the data points in hand.

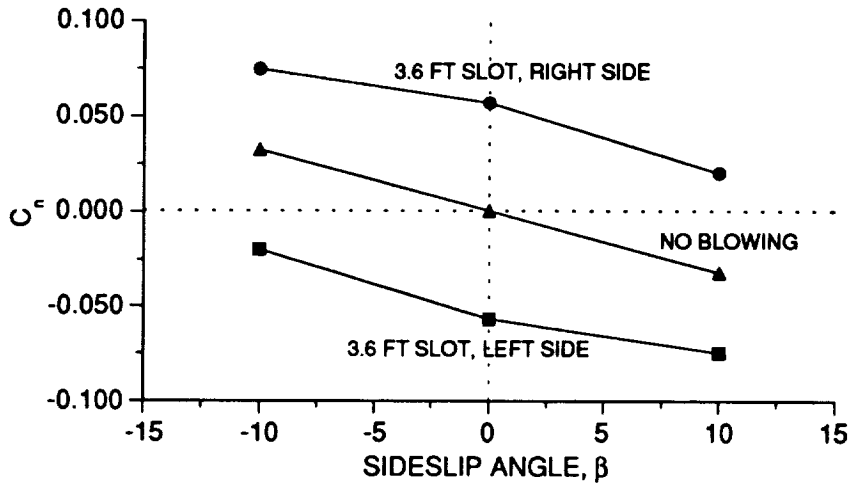

Fig. 20. Effect of sideslip angle and slot location on yawing moment coefficient. $M_\infty = 0.20$, $\alpha = 30°$, $\beta = -10°$, $Re_{\bar{c}} = 11.52 \times 10^6$.

Note that the side force due to the sideslip alone is negative (Fig. 19), whereas the yawing moment is positive (Fig. 20). This is due in part to the change in the LEX vortex structure. From Fig. 18, it was observed that the windward LEX primary vortex is displaced inboard, while the leeward LEX primary vortex is displaced outboard. Movement of the vortices causes a lower surface pressure on the windward side and a higher surface pressure on the leeward side, resulting in a side force in the negative direction. This negative force counteracts the positive side force due to the sideslip, causing a total side force in the negative direction.

This behavior can be clearly seen in the local side-force distribution along the body (Fig. 21). In the nose region, from F.S. 60.5 to F.S. 197, the side force is positive, due to the sideslip. However, in the region of the LEX, the local side force increases, then drops and becomes negative as a result of the displacement of the vortices due to the sideslip. Integrating the side force distribution results in the side-force coefficient given in Fig. 19. Since the moment center is at the base of the body (Fig. 9), the region of positive side force has a larger moment arm than the region of negative side force, thus a positive yawing moment is obtained.

Blowing in cases with sideslip yields the following results. Blowing from the right-hand side causes the side force distribution to be more positive along the entire body, whereas blowing from the left-hand side causes the side force to be more negative along the entire body, when compared to the no-blowing case. These trends are almost opposite that found in the no-sideslip case (Fig. 15). In those solutions, the side force increases in the nose region, drops off near the beginning of the LEX, and increases again. For these cases, the entire side force distribution is positive. The reason for this behavior is due in part to the interaction of the jet separation vortex with the LEX vortex.

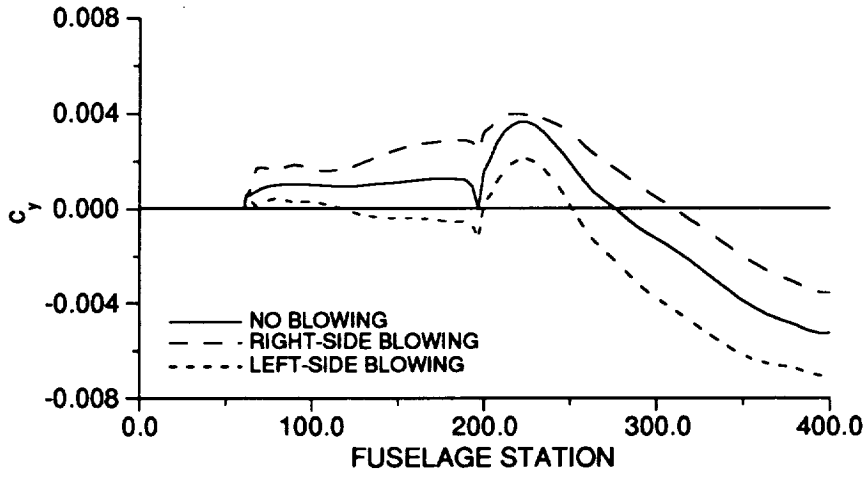

Fig. 21. Effect of sideslip and slot location on side force distribution. $M_\infty = 0.20$, $\alpha = 30°$, $\beta = -10°$, $Re_{\bar{c}} = 11.52 \times 10^6$.

As noted previously, the LEX primary vortex on the non-blowing side is weaker than the one on the blowing side (Figs. 18b,c), causing the net side force in the LEX region to be towards the blowing side. However, near the beginning of the LEX, the vortex due to the jet separation is still quite evident (Figs. 17b,c), creating a low pressure region, and thus reducing the side force to the right. In the case with sideslip and blowing from the right side, the windward LEX primary vortex is weakened by the separated jet vortex (Fig. 18b), causing a more positive side force distribution. With blowing from the left, the leeward LEX primary vortex is weakened by the separated jet vortex (Fig. 18c), causing a more negative side force distribution. These observations indicate that the interaction of the vortex structures due to the blowing with the remainder of the flow field is the primary reason for the incremental changes in the side force and yawing moment.

The solutions obtained in this part of the study are for the forebody of the aircraft only. Thus, the effects of the wing and empennage are not included. Of interest will be the effect of the forebody vortex structure due to the blowing on the vortex breakdown that is known to exist at this angle of attack. Such a breakdown does not occur in the present computations due to the lack of wings in the geometry. In order to determine how the blowing system will work on the full aircraft, experimental and computational data using the full aircraft geometry will be required.

Tangential Slot Blowing on the Isolated Forebody at Wind Tunnel Conditions

A number of experiments have been conducted using the HARV geometry with tangential slot blowing. Sub-scale water tunnel experiments[5,6] have shown the effect of blowing the vortex development about the fuselage forebody and the LEX. Full-scale wind tunnel experiments[8,9] provide force and moment data, as well as surface pressure measurements and limited flow visualization. Sub-scale wind tunnel tests[7] also provide force and moment data and surface pressure measurements. No-blowing flight data is also available from the HARV flight tests.[1]

Full-scale experimental data of the HARV with forebody tangential slot blowing were obtained in tests conducted at the Ames National Full-Scale Aerodynamics Complex 80-by-120 foot wind tunnel.[8,9] The experimental model had a 48-in. long slot, beginning 3 in. from the nose of the model, located circumferentially at $\phi = 270°$ (Fig. 5). The nominal width of the slot was 0.10 in. The slot was divided into six 8 in. sections, each section individually connected to a plenum via separate valve assemblies. Each section could be independently activated to vary the active slot length. Data for various active slot lengths and slot axial location were obtained.

Available experiment data include total aircraft forces and moments, and surface pressure distributions obtained at eight stations on the nose and LEX of the F-18 forebody (Fig. 22). The pressure data are provided by specifying the circumferential position using the angle ϕ, where ϕ has the orientation and values show in Fig. 5b. In addition, visualization of the LEX vortices was obtained in the wind-tunnel tests.

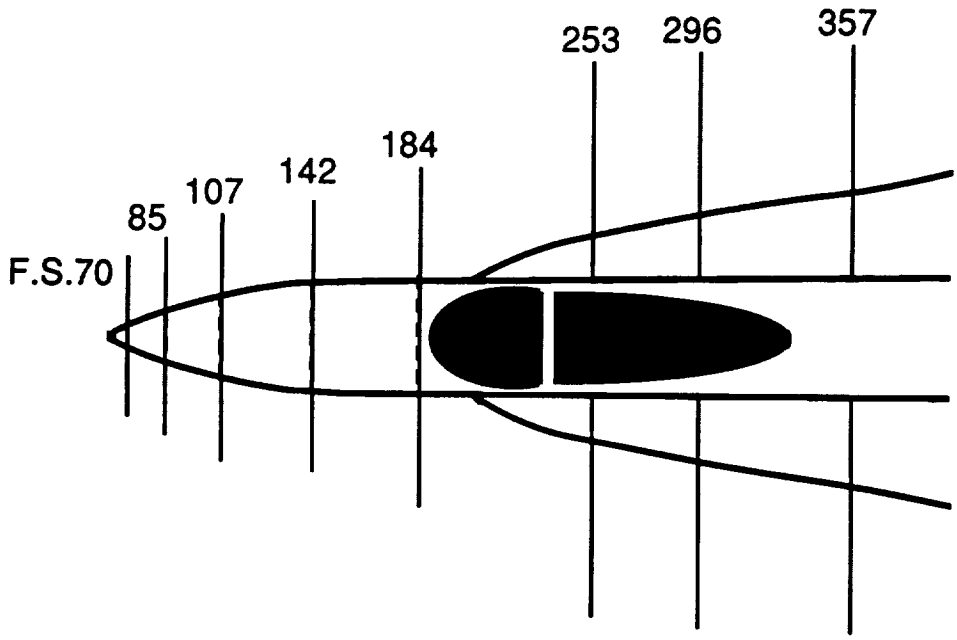

Fig. 22. Pressure tap stations on forebody of F/A-18.

The wind-tunnel pressure tap locations are identical to pressure-tap locations used in flight tests.[1] In addition, surface flow patterns were obtained in flight using dye released from the pressure port locations.[1] These patterns show the crossflow separation lines on the forebody quite clearly. Smoke flow visualization of the forebody and LEX vortices, and the LEX vortex burst location were also obtained in the flight tests.[1]

A zero-sideslip solution, with blowing, is obtained using the isolated fuselage forebody, at $M_\infty = 0.116$, $\alpha = 30.0°$, and $Re_{\bar{c}} = 9.3 \times 10^6$. These conditions correspond to full-scale wind-tunnel test conditions with $q_\infty = 20$ psf. For this case, the active slot is 32 in. long, and begins 3 in. from the nose. The jet conditions are $\dot{m} = 0.50$ lb_m/sec, $M_j = 0.64$, $T_j = 541.2°$ R, again corresponding to wind-tunnel test conditions. The isolated forebody

computations are carried out using a subset of the full-configuration overset HARV grid system.

Including the slot geometry without blowing has a local effect on the flow field, as reported in Ref. 16. The flow separates as it passes over the backward-facing step caused by the slot, then reattaches leeward of the slot. A slight pressure rise occurs in the vicinity of the slot due to this separation and reattachment (Fig. 23). Pressure station F.S. 85 lies in the slot region, with the slots located at $\phi = 90°$ and $\phi = 270°$. The computed and experimental pressure coefficient values match very well at this station, even in the vicinity of the slot. Thus, including the slot geometry improves the accuracy of the computation in the slot region.

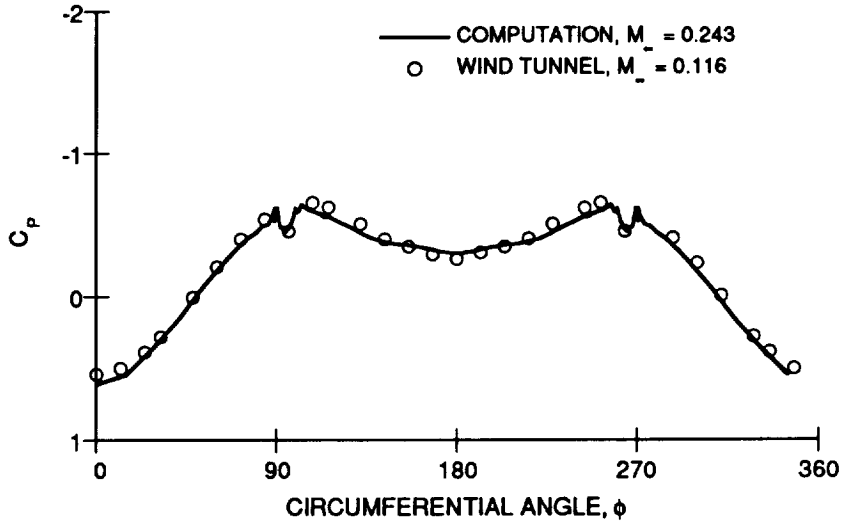

Fig. 23. Surface pressure coefficient at F.S. 85 for no blowing case with slot geometry in place.

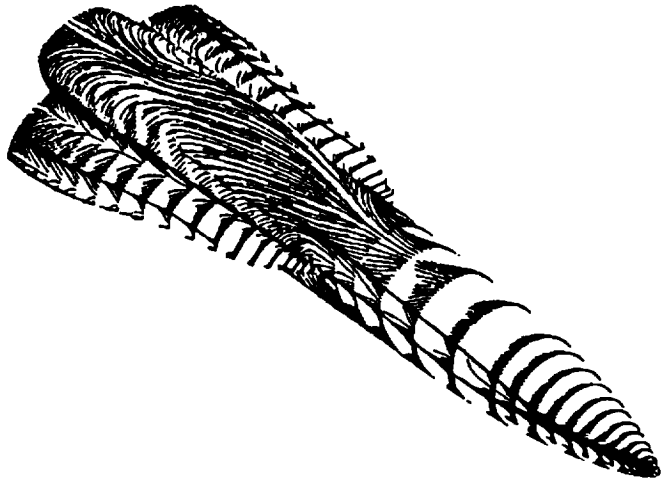

Fig. 24. Computed surface flow pattern. $M_\infty = 0.243$, $\alpha = 30.3°$, $Re_{\bar{c}} = 11.0 \times 10^6$.

The behavior of the flow due to blowing is seen from the computed surface flow pattern (Fig. 24). The surface flow pattern shows that the wall jet remains attached to the surface past the leeward symmetry plane. The wall jet separates near $\phi = 135°$. A primary crossflow separation line forms on the non-blowing side, with an attachment line between this primary crossflow separation line and the separation line due to the jet. The flow over the canopy region is altered slightly due to blowing. Although an asymmetric pressure distribution exists on the LEX (Fig. 25), the LEX secondary separation lines do not show any marked asymmetry. LEX surface oil flows were not obtained during the wind-tunnel experiment, so a comparison of the computed surface flow pattern with experimental data is not possible. These results are similar to that obtained from the solutions discussed in the previous section, indicating that the computed results are independent of the grid system used.

Figure 25 contains a comparison of the computed and measured surface pressure coefficient distributions on the F/A-18 forebody with blowing. The first two pressure stations, F.S. 70 and F.S. 85 (Fig. 25a,b), are in the active slot region. At the first pressure station, the computation resolves the sharp drop in pressure near the slot ($\phi = 270°$) measured in the experiment (Fig. 25a). This sharp drop is due to the geometry of the slot/forebody interface (Fig. 5b). The computed pressure distribution in the attached wall jet agrees qualitatively with the experimental data. The computation indicates that the wall jet separates near $\phi = 135°$. The separation is associated with a pressure drop near $\phi = 135°$ (Fig. 25b-d). The experimental jet is inferred to separate near the leeward plane of symmetry ($\phi = 180°$) from the measured pressure data; no experimental surface oil flows were obtained. The discrepancies in the pressure distributions in the slot region are believed to be caused by the algebraic turbulence model. However, note that aft of the slot region, at F.S. 142 and F.S. 184 (Fig. 25d,e), the computed pressures match the experimental values quite well.

In the LEX region, the general effect of forebody blowing is to cause a larger suction peak on the blowing-side (left) LEX (Fig. 25f-h). The stronger suction is due to an increase in the LEX vortex strength caused by blowing. The larger suction peak is seen clearly in the experimental data at F.S. 253 (Fig. 25f). At this station, the computation matches the non-blowing-side pressure better than the blowing-side pressure. At F.S. 296 and F.S. 357 (Fig. 25g,h), the experimental data do not show the large asymmetry in the pressure distribution that the computation shows. Wind tunnel visualization of the LEX vortices, due to natural condensation, shows that the blowing-side LEX vortex bursts in this region, leading to the increase in pressure over this LEX. Since the computation includes only the isolated forebody and excludes the wing and empennage, LEX vortex bursts cannot be resolved. Therefore, the surface pressure on the blowing-side LEX is lower than the non-blowing-side LEX at all three pressure stations. A computation using the full aircraft model that resolves the LEX vortex burst should lead to a better agreement with experiment at the two aft most LEX pressure stations.

Computational sectional normal- and side-force coefficients are obtained by integrating the surface pressure distributions. The corresponding experimental sectional force coefficients are obtained at the fuselage stations where sufficient pressure data were measured. The experimental sectional normal-force coefficient data indicates that blowing has little effect on the normal force (Fig. 26). The computed results indicate a larger difference, due mostly to the differences in pressure drop associated with the jet separation, since this occurs near the leeward plane of symmetry. However, the computational data follows the experimental data fairly well, indicating a gradual drop in sectional normal force along the forebody.

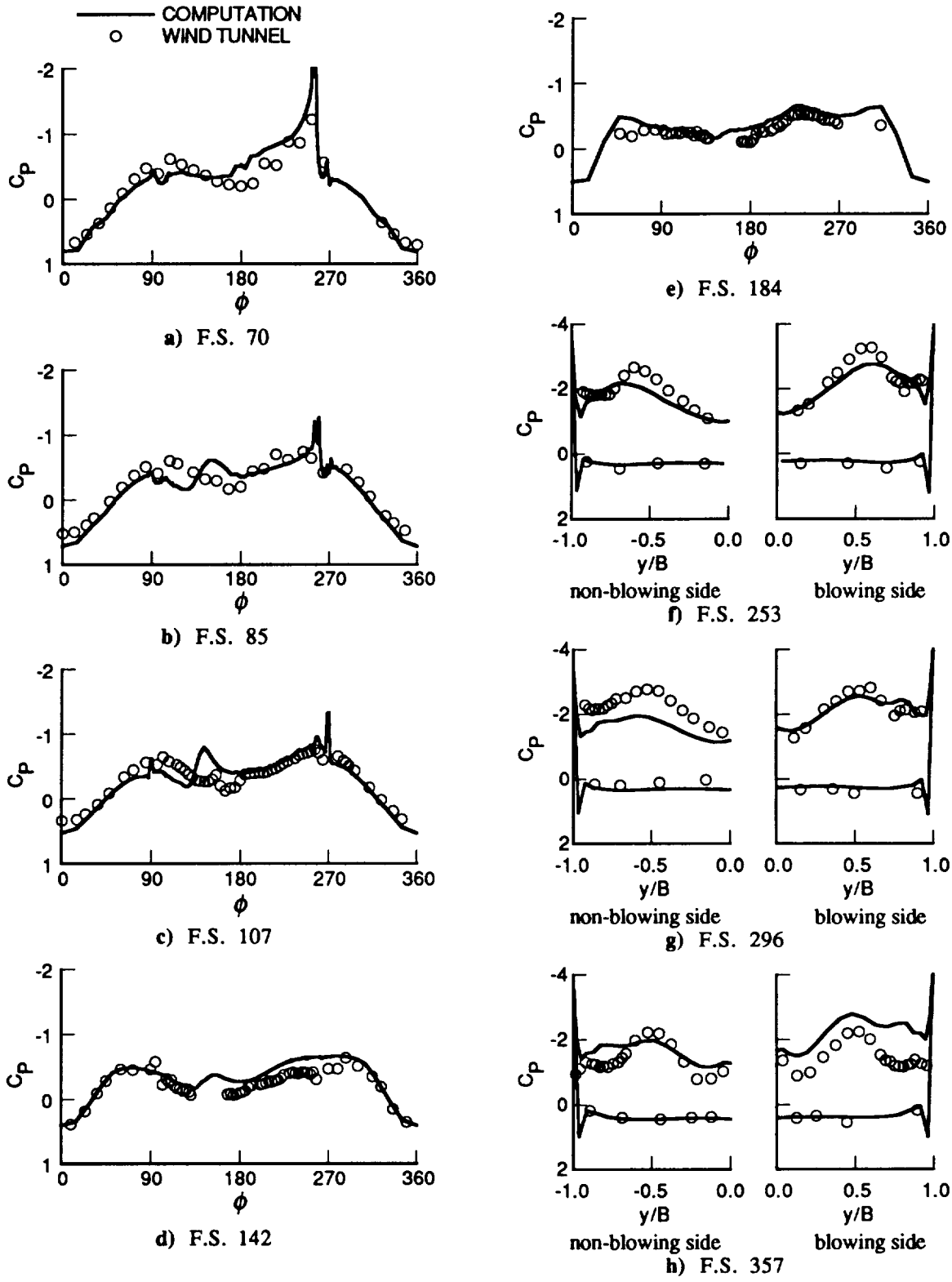

Fig. 25. Comparison of computed and experimental surface pressure coefficient. $M_\infty = 0.116$, $\alpha = 30°$, $Re_{\bar{c}} = 9.3 \times 10^6$.

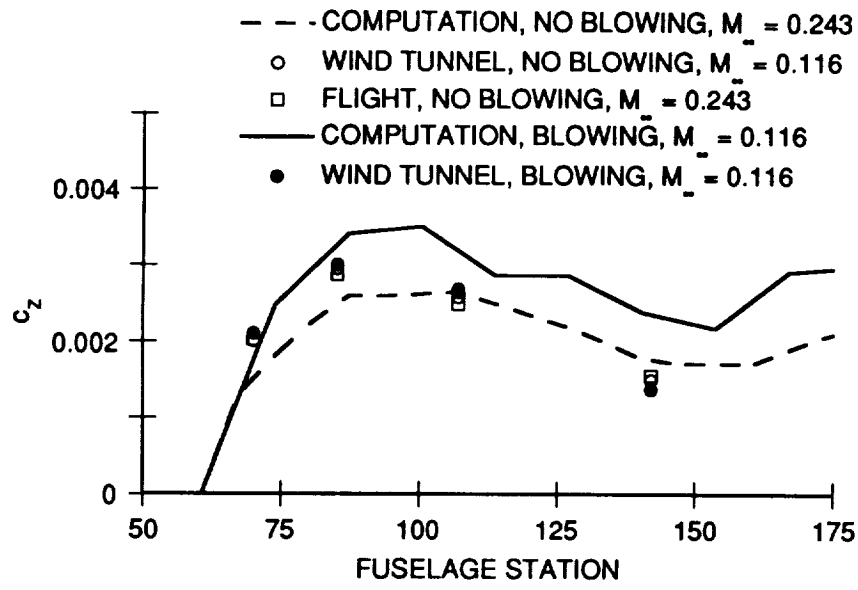

Fig. 26. Comparison of sectional normal force coefficient on the forebody.

The corresponding comparison for the sectional side-force coefficients (Fig. 27) show a larger discrepancy, although the trend of gradual increase in sectional side force along the body is the same. A more accurate computational prediction of the jet separation location should improve the side-force comparison.

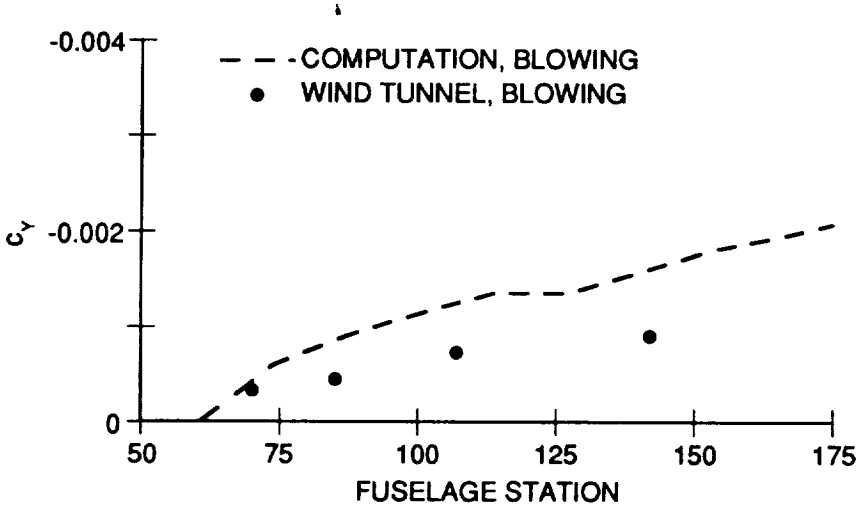

Fig. 27. Comparison of sectional side force coefficient on the forebody.
$M_\infty = 0.116$, $\alpha = 30°$, $Re_{\bar{c}} = 9.3 \times 10^6$.

Tangential Slot Blowing on the Full Aircraft

One objective of this study was to extrapolate the experimental results measured in the full-scale wind-tunnel test to actual flight-test conditions. Thus, non-time-accurate solutions for the full aircraft geometry are obtained using two slot geometries (Fig. 28). One geometry consists of an active slot length of 16 inches beginning 3 inches aft of the nose of the HARV (hereafter referred to as the 16-3 in. slot). The other geometry consists of a 16-inch long active slot beginning 11 in. aft of the nose (16-11 in. slot). The solutions are obtained at a flight condition of $M_\infty = 0.243$, $\alpha = 30.3°$, and $Re_{\bar{c}} = 11.0 \times 10^6$. The jet conditions are set such that the mass flow ratio, MFR = 1.27×10^{-4}, matching an MFR of the wind-tunnel experiment. Blowing is from the port side; therefore, the side force and yawing moment produced by blowing is directed to port and is thus negative. Non-time-accurate solutions are obtained using both geometries, and a time-accurate solution is obtained using the 16-11 in. slot.

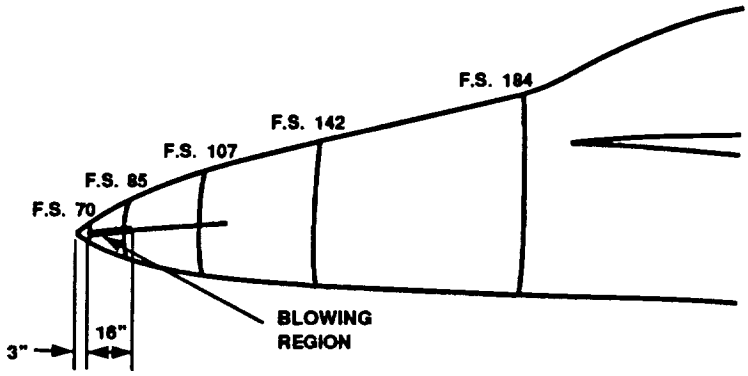

a) 16-3 in. slot

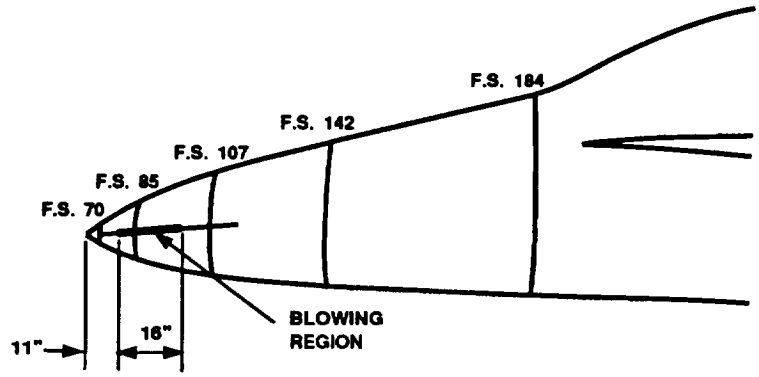

b) 16-11 in. slot

Fig. 28. Schematic of active slot geometries used in full aircraft computations.

Flow field Characteristics

The effect of blowing on the LEX vortices is seen using off-surface particle traces (Fig. 29). The non-blowing, no sideslip case reported in Ref. 4 is shown in Fig. 29a. For comparison purposes, this solution is reflected to show both sides of the aircraft, even though only half the body was used in the computation. The nose vortex becomes entrained in the LEX vortex near F.S. 300 and burst of the LEX vortex occurs near the wing/leading edge flap junction near F.S. 444. The burst vortex then impinges on the vertical tails, causing unsteady loads on the tails.

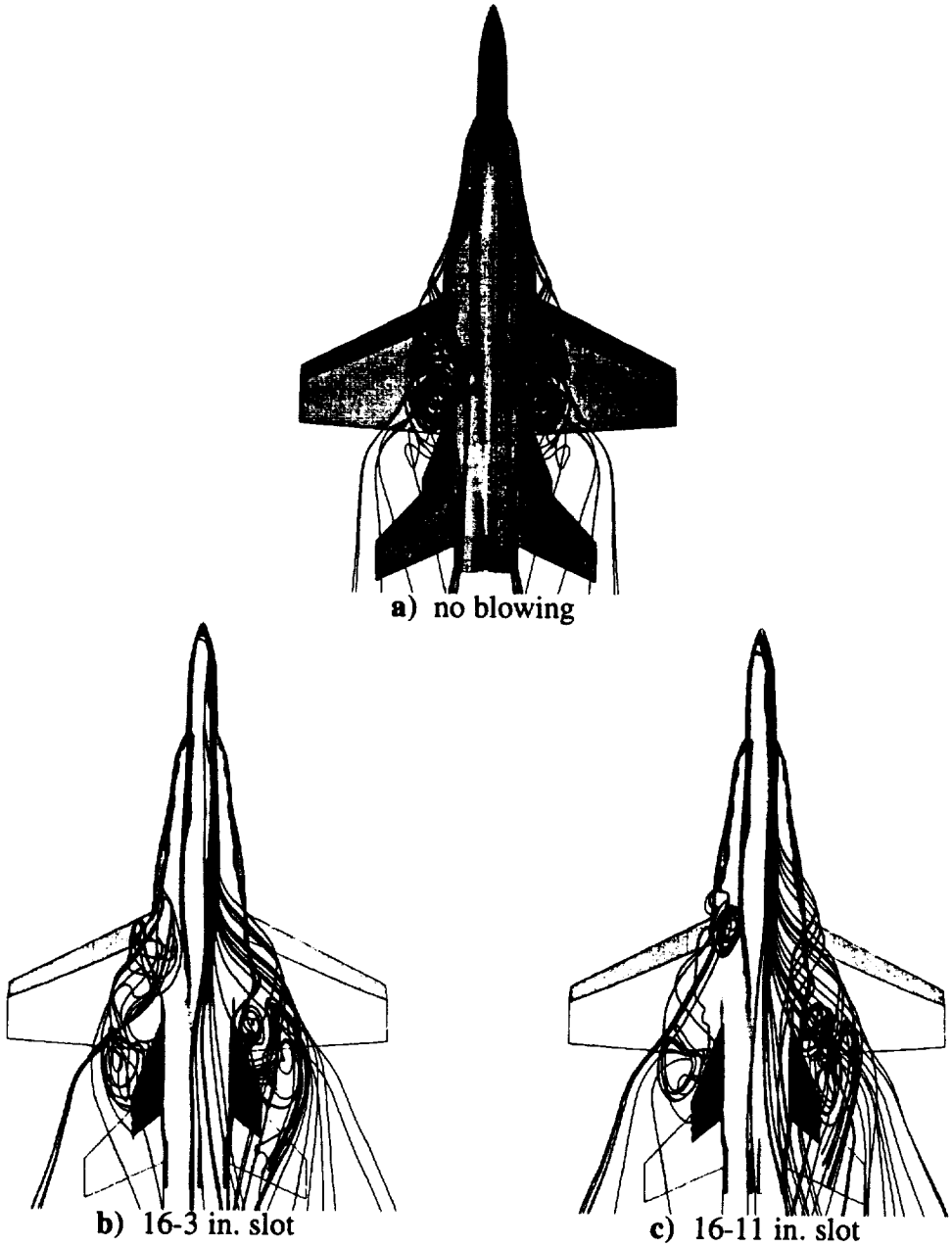

Fig. 29. Computed off-surface particle traces.
$M_\infty = 0.243$, $\alpha = 30.3°$, $Re_{\bar{c}} = 11.0 \times 10^6$, MFR = 1.27×10^{-4}.

Blowing on the pilot left changes this vortex pattern (Fig. 29b,c). Because of the jet, there is no longer any visible interaction between the vortices from the nose with the blowing-side LEX vortex. The left LEX vortex is strengthened and bursts sooner. In this case, the burst point occurs near F.S. 396. The vortex due to the separated jet interacts with the non-blowing-side LEX vortex, weakening that vortex and delaying the burst point to approximately F.S. 540, near the trailing edge of the wing. This vortex is displaced outboard by the presence of the vortex due to the separated jet. Flow visualizations from the full-scale wind tunnel tests show a similar behavior (Fig. 30). At a maximum blowing rate of $\dot{m}$ = 1.0 lb_m/sec, the blowing-side LEX vortex burst point moves forward to about F.S. 276, while the non-blowing-side LEX burst point moves aft to about F.S. 396. However, the computed burst point locations are aft of the burst point locations observed experimentally. This is due to the relatively coarse grid used in these computations, which has been shown to have an effect on the burst point location.[3] The vertical tails are immersed in the flow aft of the LEX vortex bursts.

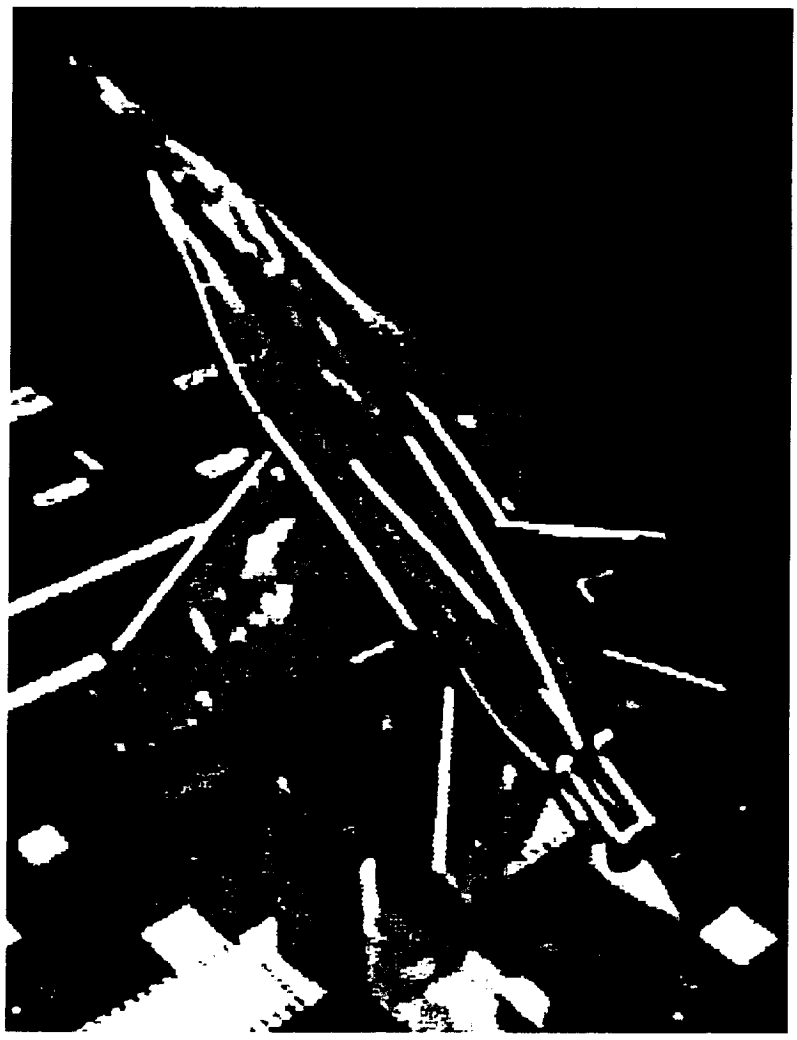

Fig. 30. Natural condensation show LEX vortex burst position in full-scale wind tunnel experiment.

On the forebody, the computed surface flow pattern shown in Fig. 31 indicates the separation line due to the jet from the 16-3 in. slot (Fig. 31a) to be closer to the leeward plane of symmetry than the separation line due to the jet from the 16-11 in. slot (Fig. 31b). Aft of the slot region, a separation line forms on the forebody. This separation line is longer in the case of the 16-3 in. slot, since the slot is located further forward on the nose.

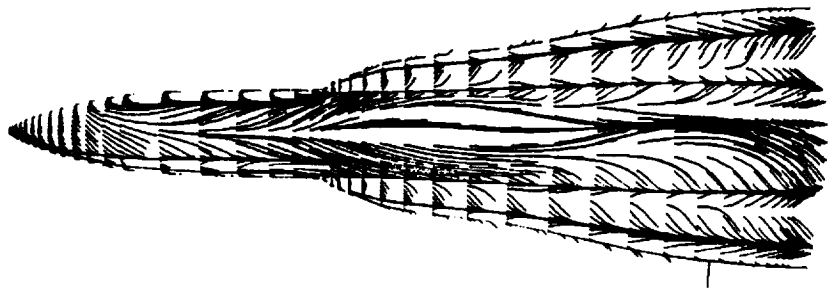

a) 16-3 in. slot

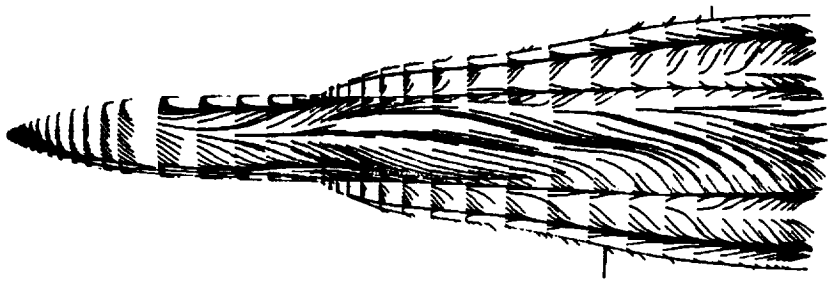

b) 16-11 in. slot

Fig. 31. Computed surface flow pattern on forebody.
$M_\infty = 0.243$, $\alpha = 30.3°$, $Re_{\bar{c}} = 11.0 \times 10^6$, MFR = 1.27×10^{-4}.

The helicity density contours[22] at F.S. 327, shown in Fig. 32, indicate the blowing-side LEX vortex to be stronger than the non-blowing-side LEX vortex, leading to the asymmetric burst point positions observed in Fig. 29. The 16-3 in. slot case (Fig. 32a) has a blowing-side LEX vortex that is slightly stronger than the blowing-side LEX vortex in the 16-11 in. slot case (Fig. 32b). However, the non-blowing-side LEX vortex in the 16-3 in. slot case is also stronger than the corresponding non-blowing-side vortex in the 16-11 in. slot solution. The helicity density contours from the isolated forebody solutions also indicate this difference in vortex strength (Fig. 13). A similar behavior was observed in computed solutions involving an ogive-cylinder with tangential slot blowing.[23,24] Indeed, Font[24] uses this behavior to identify force production mechanisms in tangential slot blowing.

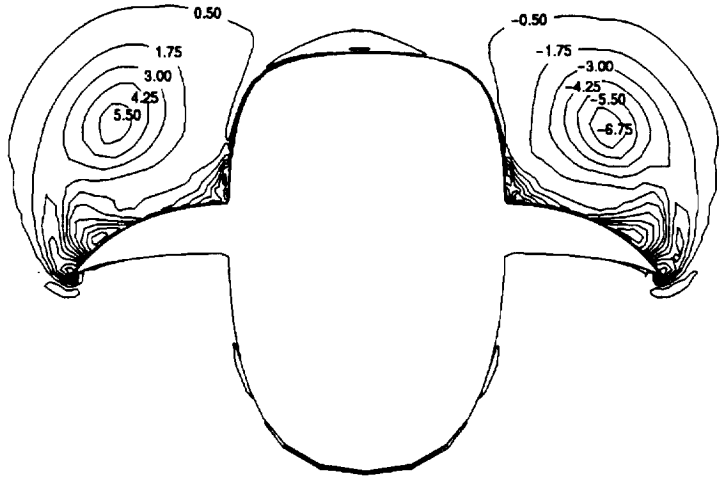

a) 16-3 in. slot

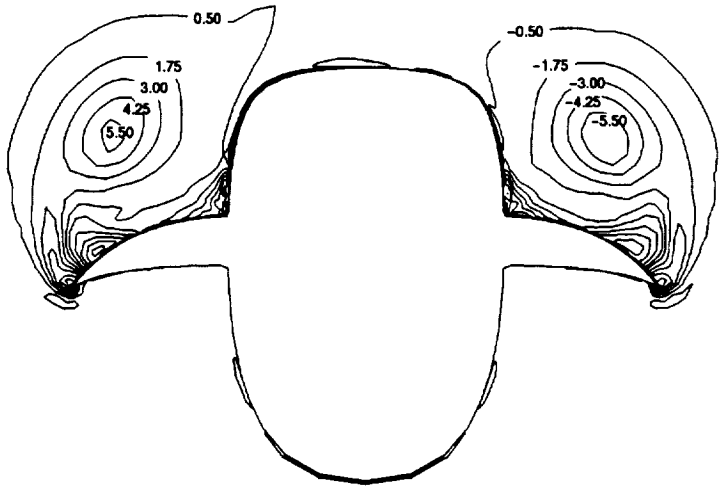

b) 16-11 in. slot

Fig. 32. Computed helicity density contours at F.S. 327.
M_∞ = 0.243, α = 30.3°, $Re_{\bar{c}}$ = 11.0 x 10^6, MFR = 1.27 x 10^{-4}.

Force Distribution Along Aircraft

Computed sectional normal- and side-force coefficient distributions are obtained over the entire aircraft. The sectional normal-force coefficient for the no-blowing and blowing computations are presented in Fig. 33. On the forebody, the normal-force distribution for the blowing case is slightly higher, as shown in the isolated forebody solution (Fig. 26). In general, however, the distribution along the body is almost identical in both cases, indicating that the total normal force coefficients for both cases are similar. This is confirmed experimentally, where the measured lift coefficient remain fairly constant for all blowing conditions.

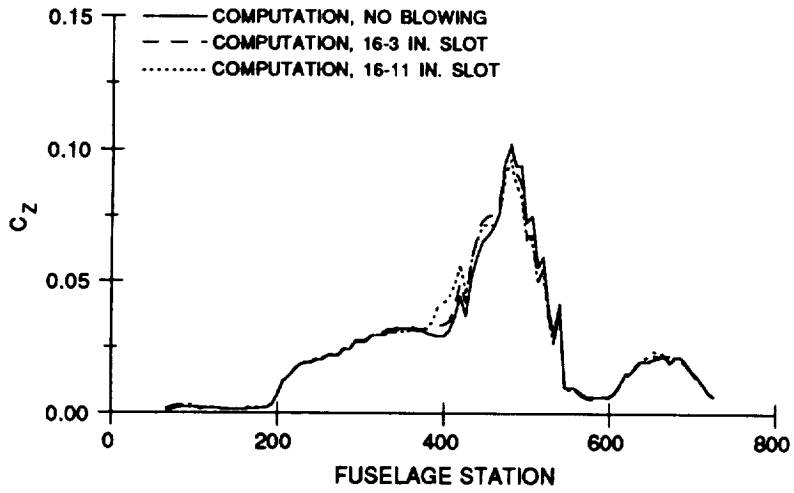

Fig. 33. Comparison of no-blowing and blowing sectional normal force coefficient. $M_\infty = 0.243$, $\alpha = 30.3°$, $Re_{\bar{c}} = 11.0 \times 10^6$, MFR = 1.27×10^{-4}.

The computed sectional side force coefficient along the body provides some interesting insights into the flow behavior (Fig. 34). In the nose region, F.S. 60.5 < x < F.S. 192, there is a negative side force due to the suction region caused by the attached jet. Along the LEX region, F.S. 192 < x < F.S. 396, there is a net negative side force due to the stronger LEX vortex on the blowing side. However, near F.S. 396, the side force becomes positive. This is due to bursting of the blowing-side vortex (Fig. 29b). The side force becomes negative as the non-blowing-side LEX vortex bursts near F.S. 540. The net result of the burst vortices impinging on the vertical tails is a negative side force, which reduces the yawing moment provided by the nose. This reduces the yawing moment that forebody tangential slot blowing can provide for a given amount of jet mass flow rate.

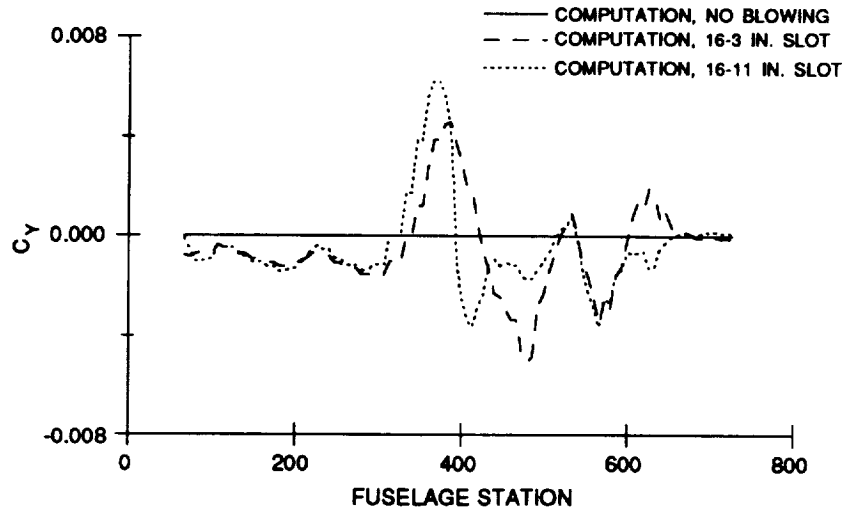

Fig. 34. Comparison of no-blowing and blowing sectional side force coefficient. $M_\infty = 0.243$, $\alpha = 30.3°$, $Re_{\bar{c}} = 11.0 \times 10^6$, MFR = 1.27×10^{-4}.

The sectional normal force distribution converged rather quickly during the computations, which are non-time-accurate (locally varying time step). After 1685 iterations, the distribution held steady over the next three hundred steps (Fig. 35). However, the sectional side force distribution fluctuates during the same three hundred step interval (Fig. 36). The forebody side force distribution remains constant forward of the LEX vortex burst point. However, aft of the burst point, the side force distribution exhibits differences over the same three hundred iteration interval. The flow aft of the vortex burst point is observed to be unsteady in both the flight tests and wind-tunnel experiments. Even though the computations are done in the non-time-accurate mode, fluctuations in the flow field still occur in the region aft of the vortex burst. The side force appears to be more sensitive to changes in the flow field in this region, since the vertical tails are fully immersed in the burst flow. For an accurate computational representation of the flow and its effect on forces and moments, time-accurate computations will be required.

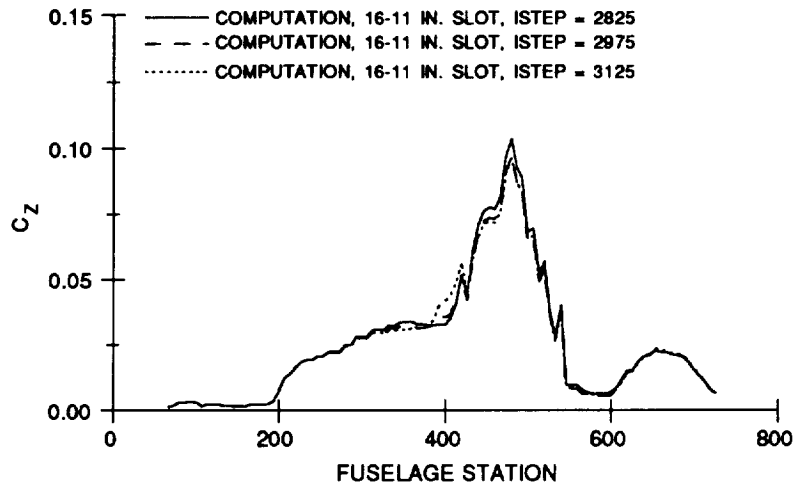

Fig. 35. Comparison of sectional normal force coefficient at various iteration levels. $M_\infty = 0.243$, $\alpha = 30.3°$, $Re_{\bar{c}} = 11.0 \times 10^6$, MFR = 1.27×10^{-4}.

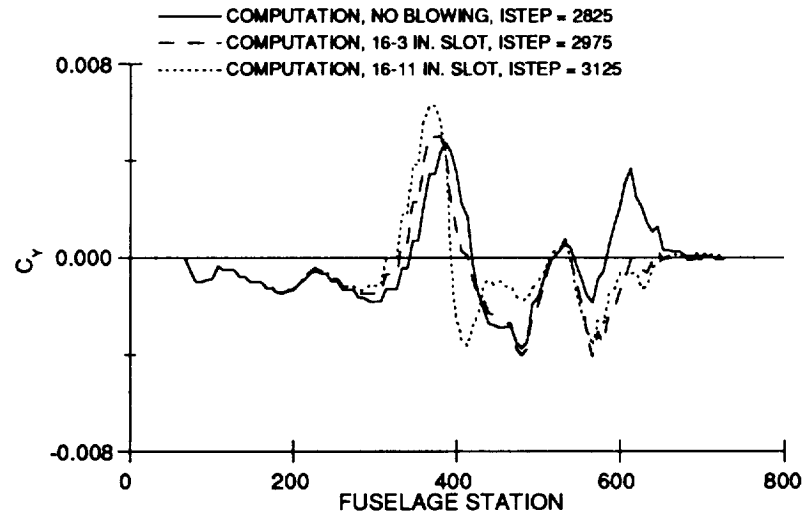

Fig. 36. Comparison of sectional side force coefficient at various iteration levels. $M_\infty = 0.243$, $\alpha = 30.3°$, $Re_{\bar{c}} = 11.0 \times 10^6$, MFR = 1.27×10^{-4}.

Moment Distribution Along Aircraft

The local yawing moment distribution along the aircraft length for both solutions is presented in Fig. 37. The local yawing moment is defined as the local sectional side force multiplied by the distance from the section to the moment center (fixed at F.S. 454). The 16-11 in. slot generates a slightly greater local yawing moment than the 16-3 in. slot in the vicinity of the active slot, up to F.S. 100. Since the radius of the forebody is greater in the region of the 16-11 in. slot, the jet creates a larger area of low pressure, leading to a greater local side force and yawing moment. In both cases, a yawing moment is produced in the region of the forebody forward of the blowing-side LEX vortex burst location, between F.S. 100 and 350, due to the difference in the strengths of the forebody and LEX vortices. The 16-11 in. slot solution shows a larger local yawing moment than the 16-3 in. slot solution in this region. This indicates the difference in vortex strength is greater in the 16-11 in. slot case, even though the 16-3 in. slot case has a stronger blowing-side LEX vortex (Fig. 32). The blowing-side surface pressure increases aft of the blowing-side LEX vortex burst; therefore, the local yawing moment becomes positive due to the low pressure produced by the still-coherent non-blowing-side LEX vortex. There is also a local yawing moment in the region of the vertical tails, aft of F.S. 525. The 16-11 in. slot solution shows a slightly more negative yawing moment in this region.

The computed local yawing moment distribution (Fig. 37) indicates that a large contribution to the total yawing moment occurs aft of the slot location. This is also evident in the blowing experiments involving the F-16[25] and the X-29.[26] The X-29 test[26] uses both a full aircraft and isolated forebody model, and the center of pressure location is quite different for the two models. It appears that although isolated forebody computations can accurately resolve the local flow features such as surface pressure (Fig. 25), full aircraft configuration computations are required to determine the full effect of blowing on force and moment generation.

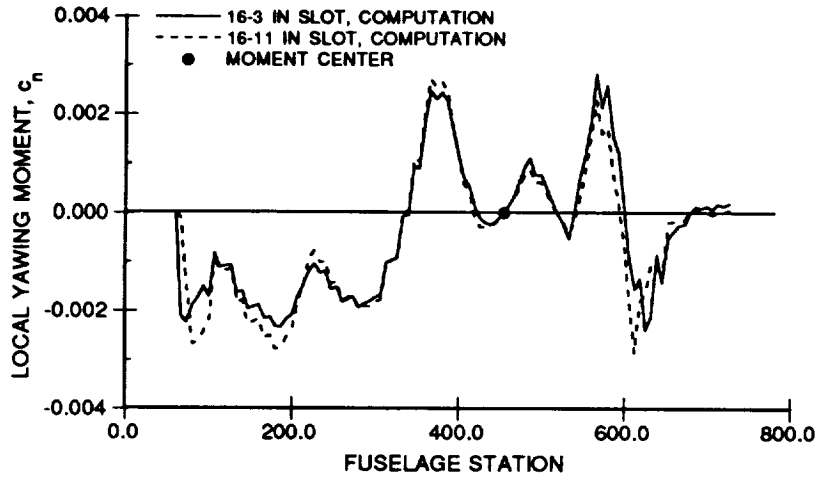

Fig. 37. Comparison of sectional yawing moment coefficient distribution. $M_\infty = 0.243$, $\alpha = 30.3°$, $Re_{\bar{c}} = 11.0 \times 10^6$, MFR = 1.27×10^{-4}.

Time-Accurate Yawing Moment Analysis

To resolve the unsteadiness in the flow field, a time-accurate solution is obtained using the 16-11 in. slot. The time-accurate solution is started from the non-time-accurate solution when the oscillatory nature of the total yawing moment is first observed. The time-accurate solution is computed using rigid vertical tails. A constant non-dimensional time step of $dt = 0.0025$ is used, which is determined by code numerical stability considerations. This time step is non-dimensionalized using the wing root chord and freestream speed of sound.

The time history of the total aircraft yawing moment is presented in Fig. 38. The yawing moment is oscillatory in nature. Also plotted in Fig. 38 is the range of values obtained during the non-time-accurate computation using the 16-11 in. slot. The non-time-accurate solution resolves the largest magnitude of the yawing moment variation fairly well. The non-time-accurate solution uses a local time step that is proportional to the grid cell size. The grid cells are small near the surface; thus, the local time step is also quite small. Since the forces and moments are obtained by integrating the surface pressure, the non-time-accurate solution should provide a fairly accurate value of the average yawing moment, even though the flow field is unsteady.

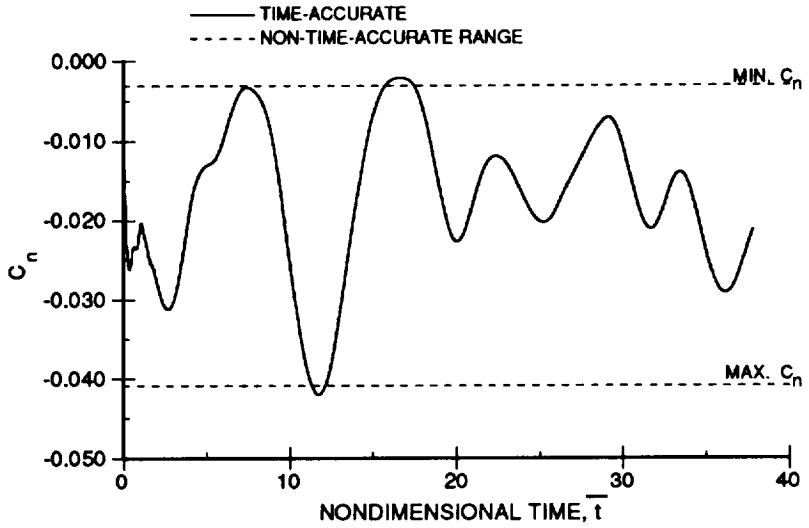

Fig. 38. Computed time history of total yawing moment.
$M_\infty = 0.243$, $\alpha = 30.3°$, $Re_{\bar{c}} = 11.0 \times 10^6$, MFR = 1.27×10^{-4}.

In the wind-tunnel test,[8] it was found that at a reduced tunnel velocity ($q_\infty = 20$ psf), the 16-11 in. slot was more effective than the 16-3 in. slot. However, at maximum tunnel velocity ($q_\infty = 33$ psf), both the 16-3 in. and 16-11 in. slots generated the same yawing moment coefficient for the same mass flow ratios. The numerical results, obtained at higher velocity flight-test conditions ($M_\infty = 0.243$), confirm the $q_\infty = 33$ psf wind-tunnel trends. A comparison of the computed total aircraft yawing moment with the full-scale wind tunnel data,[8] shown in Fig. 39, indicates that the 16-11 in. slot generates essentially the same yawing moment coefficient as the 16-3 in. slot for a given mass flow ratio, and both solutions agree fairly well with the full-scale data. Both non-time-accurate yawing moment coefficients are somewhat higher than those measured in the experiment, but this

may be due in part to the unsteadiness in the flow. The time-averaged yawing moment coefficient, obtained from the time-accurate solution, is in much closer agreement with the experimental data. The slight discrepancy may be attributed to the difference in the LEX vortex burst point locations between the computation and experiment. This result supports the notion that the mass flow ratio is a good correlation factor for tangential slots.

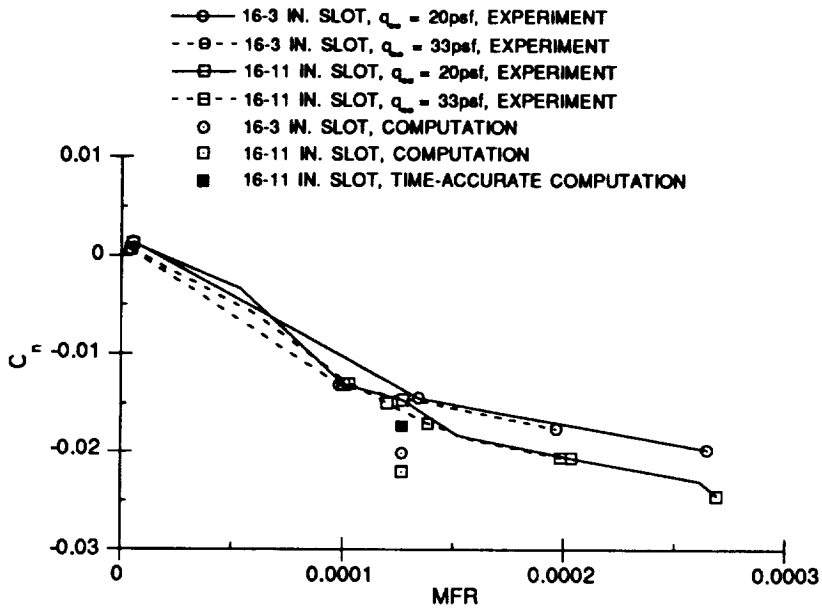

Fig. 39. Comparison of total yawing moment.

Effect of Vertical Tails on Aircraft Yawing Moment

Figure 40 presents the local yawing moment distribution along the body for two instants in time, one taken at a local maximum yawing moment point ($\bar{t}$ = 20.25 in Fig. 38), and the other taken at a local minimum yawing moment point ($\bar{t}$ = 22.69 in Fig. 38). The effect of the vertical tails on the total yawing moment is evident in this figure. The flow over the forebody and LEX region forward of the blowing-side LEX vortex burst is essentially steady, since the local yawing moment does not change with time. There is, however, a large difference in the local yawing moment in the vertical tail region. At $\bar{t}$ = 20.25, the vertical tails generate a negative yawing moment, thus increasing the total yawing moment. At $\bar{t}$ = 22.69, the vertical tails generate a positive yawing moment, thus reducing the total yawing moment produced by blowing. In the X-29 wind tunnel experiment,[26] the single vertical tail was shown to have an influence on the side force and yawing moment, although at 30° angle of attack, the influence was minor. However, in the case of the HARV, with the twin vertical tails fully immersed in the unsteady flow aft of the LEX vortex bursts, the effect of the vertical tails is expected to be larger.

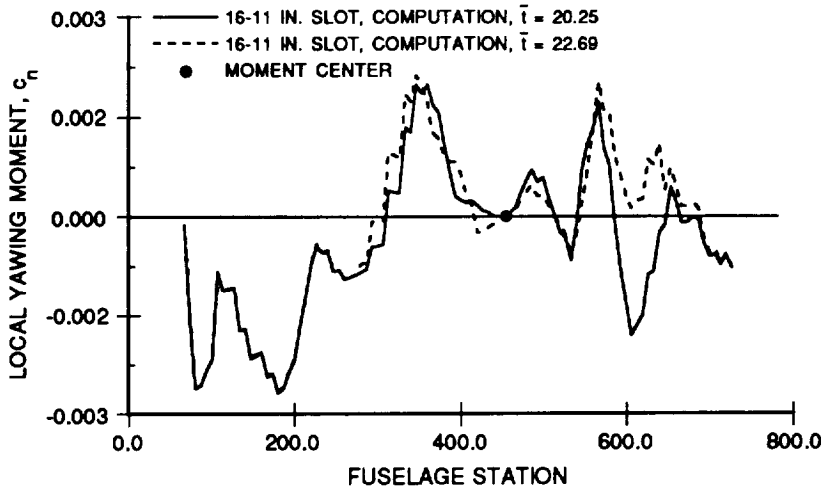

Fig. 40. Computed sectional yawing moment distribution at two points in the time history.
$M_\infty = 0.243$, $\alpha = 30.3°$, $Re_{\bar{c}} = 11.0 \times 10^6$, MFR = 1.27×10^{-4}.

Analysis of Vertical Tail Aerodynamic Loads

The time history of the side force on the vertical tails is presented in Fig. 41. Since the tails are aft of the moment center, a positive side force on either tail generates a negative contribution to the total aircraft yawing moment. In Fig. 41, the positive side force on the blowing-side (port) tail increases the total aircraft yawing moment, while the negative side force on the non-blowing-side (starboard) tail decreases the total aircraft yawing moment. The fluctuations in the tail loading appear to be out of phase, such that as the magnitude of the side force increases on one tail it decreases on the other. This, in turn, leads to the change in local yawing moment in the vertical tail region observed in Fig. 40.

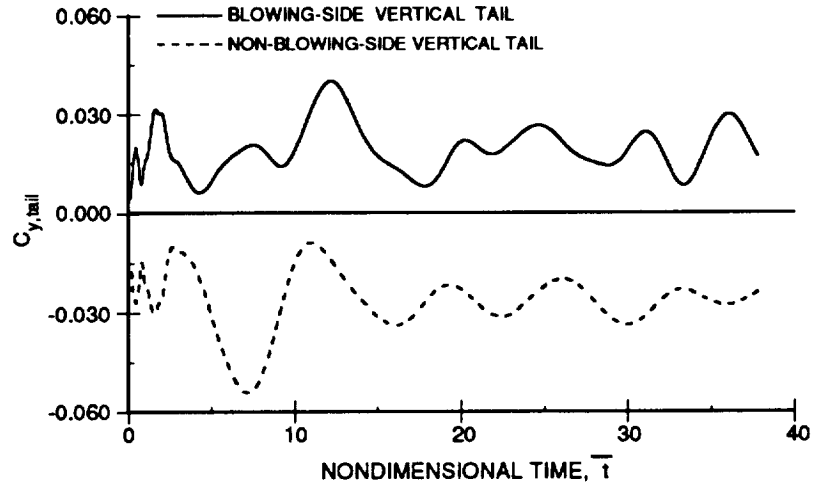

Fig. 41. Comparison of computed vertical tail side force time histories.

The bending moments applied to the vertical tails due to the aerodynamic forces are computed and presented in Fig. 42. the bending moment center is taken to be the root of the vertical tail. A Fast Fourier Transform analysis is performed on this data (Fig. 43) using 8192 steps. The Fast Fourier Transform shows a frequency peak in the blowing-side tail bending moment loads at 9 Hz. The bending moment applied to the non-blowing-side vertical tail has a dominant frequency at 12 Hz. Compared to the frequency obtained in previous computations about the F-18 geometry without blowing,[4,27] and various experiments[28-30] (Fig. 44), it appears that blowing decreases the dominant frequency of the airloads slightly, thus moving away from the first bending natural frequency of the vertical tails, which was found to be about 15 Hz.[28] Since blowing affects the frequency content of the unsteady flow aft of the vortex burst, blowing has the potential to control tail buffet on the F-18 in a manner similar to that used on a rounded leading-edge delta wing.[31] In the delta wing case, symmetric tangential leading-edge slot blowing was used to reduce tail buffet by effectively changing the angle of attack of the wing.

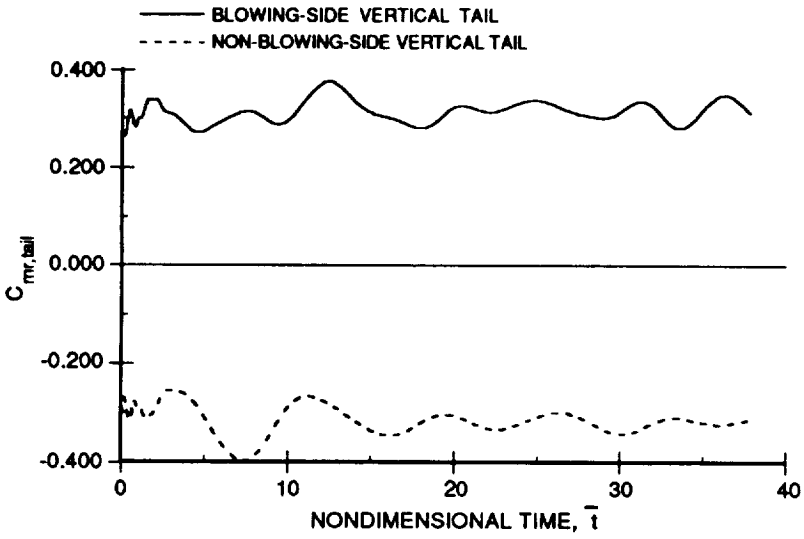

Fig. 42. Comparison of computed vertical tail bending moment time histories.

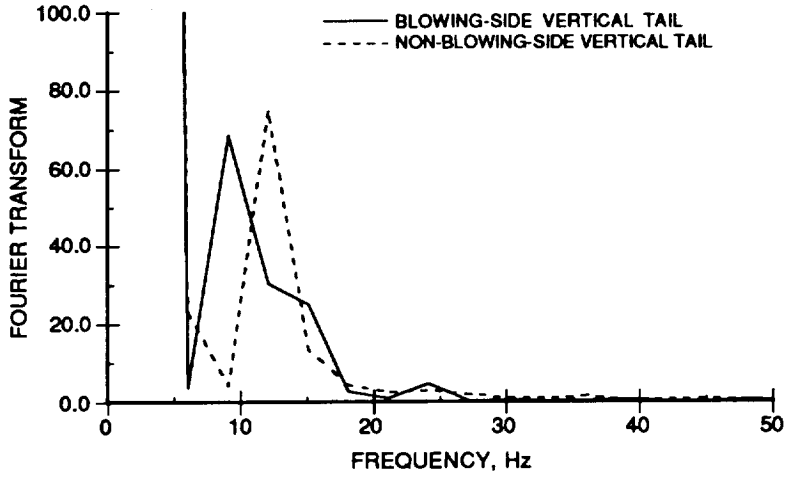

Fig. 43. Fast Fourier Transform of computed vertical tail bending moment time histories.

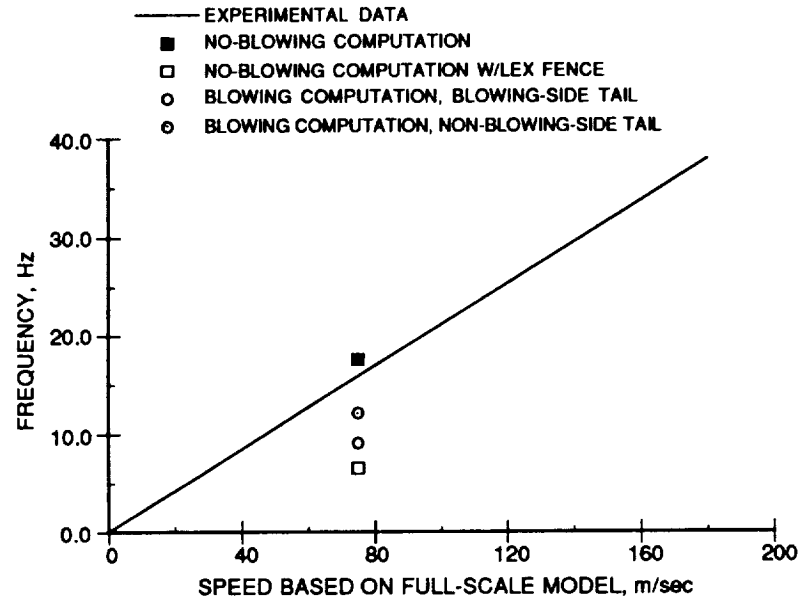

Fig. 44. Computed dominant frequencies in flow field and experimental tail buffet frequency data.

Effect of Freestream Mach Number on Blowing

One objective of the computational investigation is to determine the effect of freestream Mach number on the efficiency of tangential slot blowing. Therefore, computed no-blowing and blowing solutions are obtained for flow about an isolated F-18 forebody at $\alpha = 30.3^{\circ}$ at three different freestream Mach numbers, $M_\infty = 0.243$, 0.400, and 0.700. The corresponding Reynolds numbers, based on the F/A-18 wing mean aerodynamic chord, are $Re_{\bar{c}} = 11.0 \times 10^6$, 18.0×10^6, and 31.4×10^6, respectively.

No-Blowing Solutions

No-blowing solutions are obtained at each freestream Mach number and serve as baseline solutions from which the blowing solutions are computed. Analysis of the no-blowing solutions also serve as a check to insure that the numerical method is accurately predicting the flow fields and the relevant trends. Although details of the flow field are similar to results presented in a previous section, the main features are briefly discussed for comparison with the blowing results.

Flow Field Characteristics

Figure 45 shows the surface flow pattern and off-surface instantaneous streamlines obtained from the solution computed at $M_\infty = 0.700$. The flow field is similar to that reported in previous work with the isolated F/A-18 forebody at a lower freestream Mach number. There are a primary and secondary separation line on each side of the forebody barrel. Flow which separates from the forebody rolls up to form vortices above the forebody (Fig. 45b). Each wing leading edge extension (LEX) has a sharp leading edge and a primary crossflow separation line lies along this edge. A secondary separation line is also evident on the upper surface of each LEX (Fig. 45a). At this angle of attack, the no-blowing flow field is symmetric.

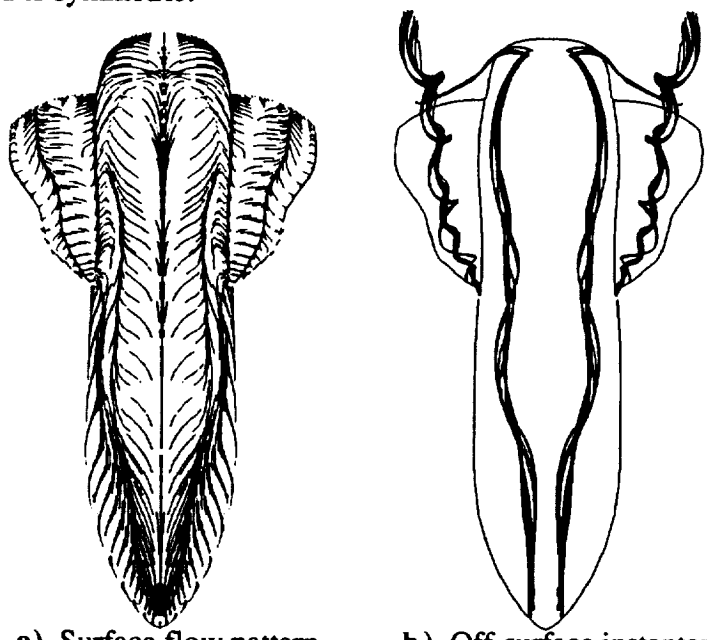

a) Surface flow pattern

b) Off-surface instantaneous streamlines

Fig. 45. Flow field characteristics, $M_\infty = 0.700$, $\alpha = 30.3^{\circ}$, $Re_{\bar{c}} = 31.4 \times 10^6$.

Surface Pressure Coefficient Comparison

Figure 46 shows a comparison of the computational and experimental[32] spanwise surface pressure distributions for the two higher Mach number cases at three axial locations on the LEX. Experimental data show a reduction in the suction peaks with increasing freestream Mach number.[32] This trend is also evident in the computational results. The computation obtained at $M_\infty = 0.400$ underpredicts the suction peaks on the LEX. However, the comparison of the data for $M_\infty = 0.700$ is quite good, especially at the upstream LEX stations, F.S. 253 and F.S. 296. The comparison worsens slightly at F.S. 357.

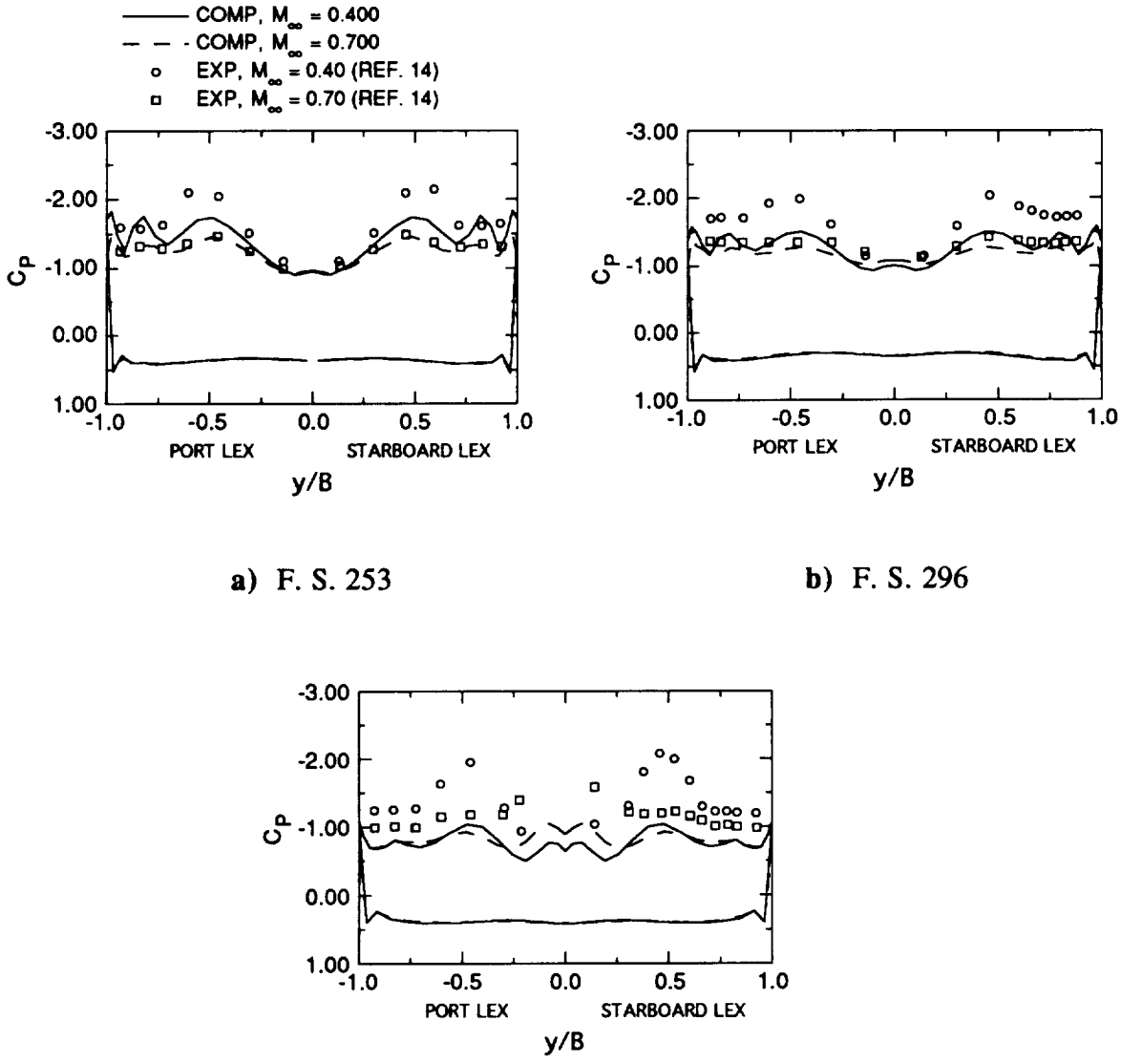

a) F. S. 253

b) F. S. 296

c) F. S. 357

Fig. 46. Comparison of computed surface pressure coefficient; $\alpha = 30.3°$.

The underprediction of the LEX suction peaks at the lower Mach number may be due to the use of the isolated forebody in the computations. Results shown earlier using the isolated forebody at wind tunnel test conditions also underpredict the surface pressure coefficient. However, addition of the wing and tail geometry produced a better comparison with flight test data.[4] By including the wing and tail, LEX vortex burst is resolved. This affects the surface pressure, especially on the last pressure station, F.S. 357, since the burst occurs in this region. The comparison at the higher freestream Mach number is better since at the higher Mach number, the influence of downstream effects on the flow at a given axial location is reduced. The overall good agreement in the trends with increasing Mach number shown in the no-blowing solutions provide confidence that the analogous trends seen in the computed blowing solutions will also be valid.

Table 1. Jet exit conditions used in computational study.

16 inch slot starting 11 inches from the nose (16-11 in. slot)

M_∞	$\dot{m}$ (lb/sec)	MFR (x 10^{-3})	M_{jet}	P_{tot} (lb/in^2)	T_{tot} (°R)	P_e/P_a
0.243	0.056	0.015	0.125	5.65	402.	1.00
0.243	0.111	0.03	0.248	5.83	405.	1.00
0.243	0.224	0.06	0.50	6.63	420.	1.00
0.243	0.432	0.12	0.96	10.14	473.	1.00
0.243	0.668	0.18	1.00	15.76	480.	1.49
0.243	0.868	0.24	1.00	20.49	480.	1.94
0.400	0.187	0.03	0.43	6.15	415.	1.00
0.400	0.368	0.06	0.85	8.68	460.	1.00
0.400	0.714	0.12	1.00	16.84	480.	1.64
0.400	1.098	0.18	1.00	25.90	480.	2.53
0.400	1.427	0.24	1.00	33.68	480.	3.29
0.700	0.323	0.03	0.76	7.78	447.	1.00
0.700	0.639	0.06	1.00	15.10	480.	1.50
0.700	1.248	0.12	1.00	29.44	480.	2.93
0.700	1.871	0.18	1.00	44.17	480.	4.40
0.700	2.495	0.24	1.00	58.89	480.	5.86

24 inch slot starting 3 inches fro m the nose (24-3 in. slot)

M_∞	$\dot{m}$ (lb/sec)	MFR (x 10^{-3})	M_{jet}	P_{tot} (lb/in^2)	T_{tot} (°R)	P_e/P_a
0.243	0.056	0.015	0.081	5.62	401.	1.00
0.243	0.111	0.03	0.162	5.69	403.	1.00
0.243	0.224	0.06	0.325	6.04	409.	1.00
0.243	0.432	0.12	0.63	7.36	432.	1.00
0.243	0.668	0.18	0.96	10.21	475.	1.00
0.243	0.868	0.24	1.00	13.33	480.	1.26
0.400	0.187	0.03	0.28	5.71	407.	1.00
0.400	0.368	0.06	0.55	6.67	425.	1.00
0.400	0.714	0.12	1.00	10.97	480.	1.07
0.400	1.098	0.18	1.00	16.94	480.	1.66
0.400	1.427	0.24	1.00	21.94	480.	2.14
0.700	0.323	0.03	0.50	6.25	420.	1.00
0.700	0.639	0.06	1.00	9.86	480.	1.01
0.700	1.248	0.12	1.00	19.10	480.	1.92
0.700	1.871	0.18	1.00	28.75	480.	2.88
0.700	2.495	0.24	1.00	38.40	480.	3.85

Blowing Solutions

Solutions with blowing are obtained at each freestream Mach number using two active slot configurations. One configuration consists of a 16 in. active slot beginning 11 in. aft of the nose (hereafter referred to as the 16-11 in. slot). The other slot configuration has a 24 in. slot beginning 3 in. aft of the nose (24-3 in. slot). Blowing occurs only on the port side (pilot's view) of the forebody. For each slot configuration and freestream Mach number, solutions are obtained at five mass flow ratios (MFR) ranging from 0.03 x 10^{-3} to 0.24 x 10^{-3} (Table 1). At M_∞ = 0.243, additional cases are computed for MFR = 0.015 x 10^{-3}. The results permit evaluation of the effect of varying Mach number, at a fixed MFR, on the efficiency of tangential slot blowing, as well as the effect of varying MFR at a fixed Mach number.

Yawing Moment Comparison

The yawing moment, C_n, obtained from blowing is plotted against MFR for both slot configurations in Fig. 47. The moment center used to compute C_n is located at the center of gravity point of the aircraft, F.S. 454. As was seen previously in sub-scale[7] and full-scale[8] wind-tunnel tests, the mass flow ratio is a good parameter for correlating the forces produced by blowing at differing flow conditions.

The computed results show that both slots configurations are capable of generating yawing moment, even at transonic maneuvering Mach numbers. For both slot configurations at M_∞ = 0.243 and 0.400, the yawing moment increases with increasing MFR. For the case with the 16-11 in. slot at M_∞ = 0.700, the yawing moment first increases, then levels off and decreases slightly as the MFR increases. A similar, but less pronounced, leveling off of C_n also occurs for the 24-3 in. slot at M_∞ = 0.700. However, useful yawing moments are obtained at moderate jet mass flow rates at all freestream Mach numbers (Table 1). Further analysis of the computed flow fields yields information about the flow physics associated with the behavior of the curves shown in Fig. 47.

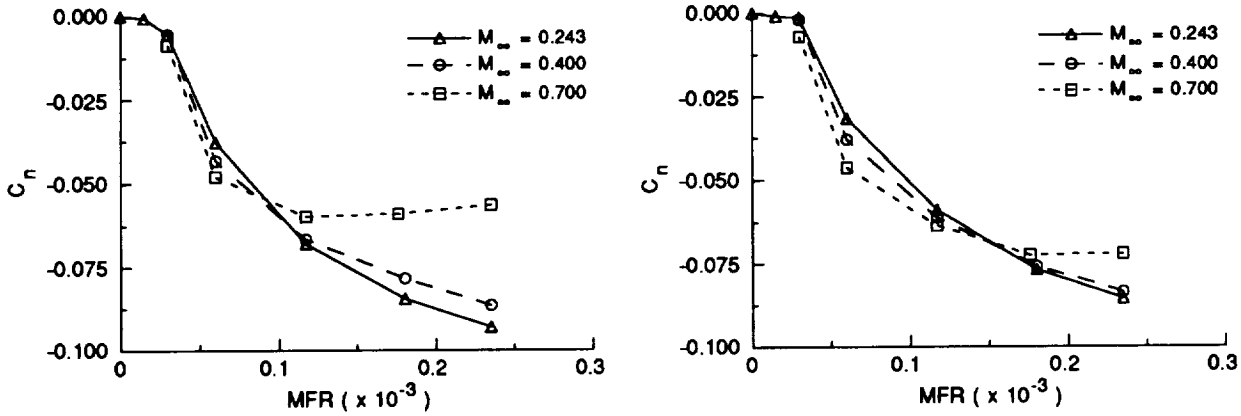

a) 16-11 in. slot

b) 24-3 in. slot

Fig. 47. Computed yawing moment plotted against MFR for isolated forebody with blowing; α = 30.3°.

At the lowest blowing rate analyzed, MFR = 0.015 x 10^{-3}, almost no yawing moment is obtained for either slot configuration. This is consistent with the sub-scale results obtained by Kramer et al.[7] At this angle of attack, no force reversal was observed in either the experimental or computational data.

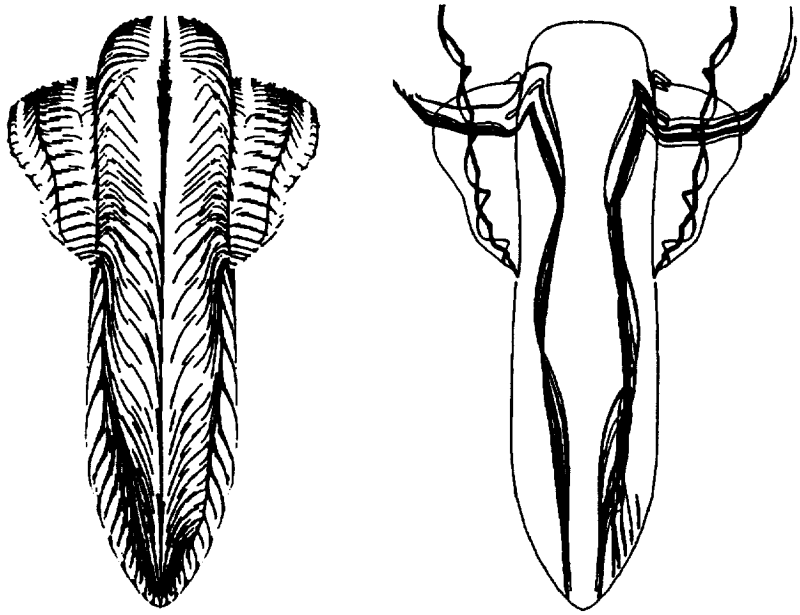

a) Surface flow pattern

b) Off-surface instantaneous streamlines

Fig. 48. Flow field characteristics at low blowing rates. $M_\infty = 0.243$, $\alpha = 30.3°$, $Re_{\bar{c}} = 11.0 \times 10^{-6}$, MFR = 0.015 x 10^{-3}, 16-11 in. slot.

The computed surface flow pattern and off-surface instantaneous streamlines, obtained from the 16-11 in slot, $M_\infty = 0.243$, MFR = 0.015 x 10^{-3} solution (Fig. 48), show the jet separating along with the blowing-side primary forebody vortex. There is no change in the position of the blowing-side primary separation line on the forebody barrel (Fig. 48a). The off-surface instantaneous streamlines (Fig. 48b) show the jet to have almost no effect on the position of either the blowing-side or non-blowing-side forebody vortex. The early separation reduces the low pressure region caused by the attached jet and reduces the interaction of the jet with the non-blowing-side forebody vortex. Both of these effects serve to reduce the amount of side force and yawing moment generated.

At MFR = 0.03 x 10^{-3}, blowing from the 16-11 in. slot generates slightly higher amounts of C_n than blowing from the 24-3 in. slot. The smaller area of the 16-11 in. slot requires a higher jet exit Mach number to obtain a given jet mass flow rate. The higher jet exit velocity increases the suction pressure generated by the attached portion of the jet. This serves to increase the yawing moment generated by blowing.

At MFR = 0.06 x 10^{-3}, the yawing moment increases slightly with increasing freestream Mach number. This is most evident in the 24-3 in. slot configuration results. Again, this is due to the differences in the jet exit Mach numbers (Table 1). As the freestream Mach number increases, the jet mass flow rate must increase to maintain a given MFR value. An

increase in jet mass flow rate causes a corresponding increase in the jet exit Mach number until choked conditions are reached at the slot exit.

Once the jet is choked, the effectiveness of blowing depends upon the jet exit pressure. The ratio of the jet exit pressure, P_e, to the local static pressure, P_a, is presented in Table 1. For moderate values of this ratio, $P_e/P_a < 1.5$, C_n increases with MFR and does not depend on the freestream Mach number. This can be seen in 24-3 in. slot results for $0.12 \times 10^{-3} < \text{MFR} < 0.24 \times 10^{-3}$. However, for $P_e/P_a > 1.5$, the blowing effectiveness levels off. This is most evident in the 16-11 in. slot, $M_\infty = 0.700$ case. As the blowing rate, and thus the jet exit pressure, increases, the yawing moment levels off and slightly decreases for this case. This is due to the phenomenon of overblowing.

Overblowing has been observed experimentally[7] as a drop-off of yawing moment at high blowing rates. The effect of overblowing on the computed flow field is observed by plotting the velocity vectors in a crossflow plane at F.S. 85 that passes through the jet region (Fig. 49). Overblowing occurs when the jet flow is sonic and underexpanded ($P_e/P_a > 1.0$) at the slot exit. For $P_e/P_a > 1.5$, the jet rapidly expands after leaving the slot, deflecting the flow away from the fuselage surface, causing earlier crossflow separation. This action negates the Coanda effect, which causes delay of the crossflow separation. At the lower blowing rate (Fig. 49a), the jet remains attached to the surface. As the jet negotiates the curvature of the surface, the surface pressure drops, generating a low pressure region, contributing to the side force and yawing moment generated. However, in a case with overblowing, the jet does not remain attached to the surface (Fig. 49b). Rather, it separates and rides on top of a layer of fluid that is moving in the opposite direction. The separation of the jet reduces the suction generated by the jet, thereby reducing the side force and yawing moment. Side force and yawing moment are still generated due to the manipulation of the forebody vortices by the jet.

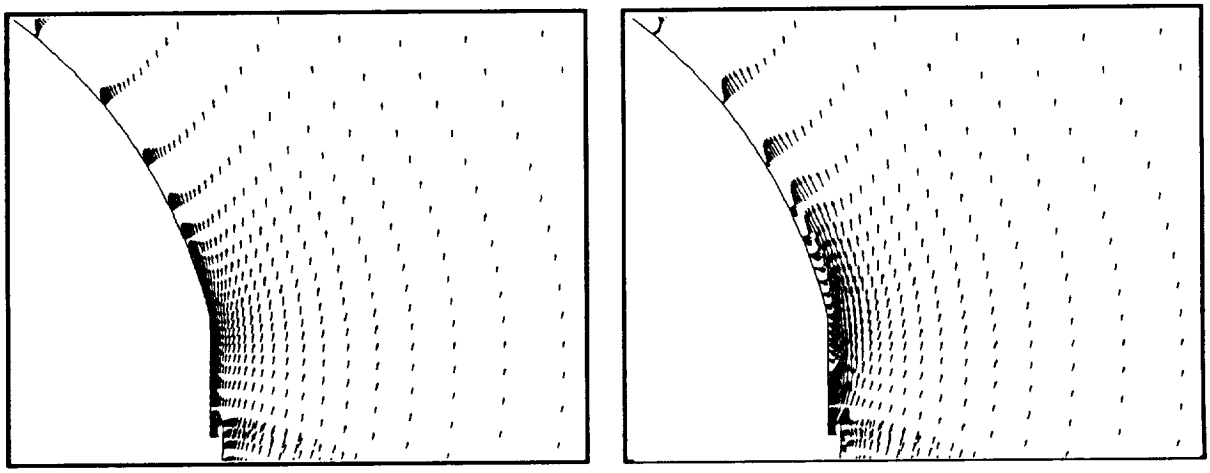

a) MFR = 0.06×10^{-3}, $P_e/P_a = 1.50$ b) MFR = 0.24×10^{-3}, $P_e/P_a = 5.86$

Fig. 49. Effect of overblowing on flow in vicinity of the slot; computed velocity vectors in the crossflow plane at F.S. 85.
$M_\infty = 0.700$, $\alpha = 30.3°$, $Re_{\bar{c}} = 31.4 \times 10^6$, 16-11 in. slot.

The behavior of the overblown jet is observed graphically using instantaneous streamlines to illustrate the vortices formed on the nose and the jet (Fig. 50). For the attached jet flow (Fig. 50a), blowing causes the nose vortex on the blowing side to merge with the nose vortex on the non-blowing side. The jet flow also becomes entwined in this merged nose vortex. In the overblown case (Fig. 50b), the two nose vortices do not merge, although there is still a slight interaction between the jet flow and the non-blowing-side nose vortex. This is in contrast to the very low blowing case (Fig. 48b), where no interaction between the jet and non-blowing-side forebody vortex is observed.

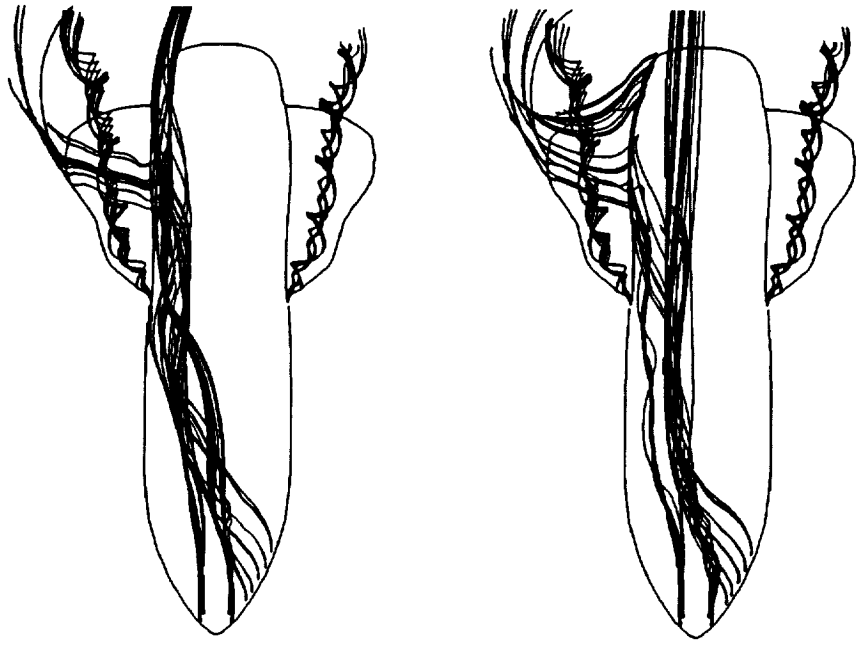

a) MFR = 0.06 x 10^{-3}, P_e/P_a = 1.50 **b)** MFR = 0.24 x 10^{-3}, P_e/P_a = 5.86

Fig. 50. Off-surface instantaneous streamlines with blowing. $M_\infty = 0.700$, $\alpha = 30.3°$, $Re_{\bar{c}} = 31.4 \times 10^6$, 16-11 in. slot.

The behavior of the jet also has an effect on the contribution of the forebody barrel and LEX region to the yawing moment. This effect can be seen in Fig. 51, which presents the local yawing moment distribution along the forebody. The computational results shown in the previous sections indicate that there is a contribution to the side force and yawing moment from the forebody barrel aft of the slot and the LEX region. At the lowest blowing rate shown, there is almost no yawing moment evident along the entire forebody. This is due in part to the early separation of the jet. Without this flow interacting with the non-blowing-side LEX vortex, changes in the surface pressure in the LEX region is reduced. Overblowing reduces the amount of yawing moment obtained in the blowing region as well as over the remainder of the forebody. Again, this is due to the early separation of the jet and the limited interaction between the jet and the non-blowing-side nose and LEX vortices.

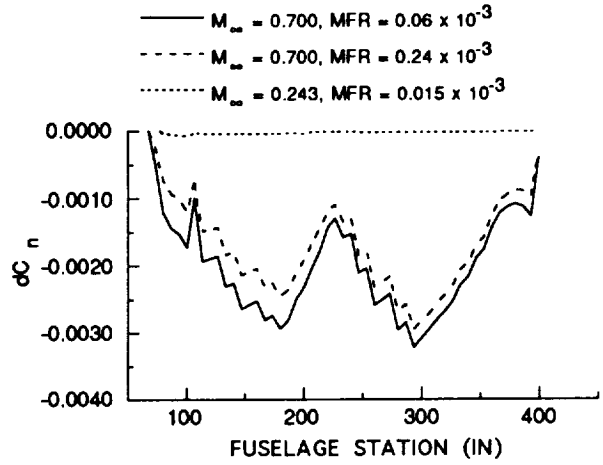

Fig. 51. Computed local yawing moment distribution with blowing, 16-11 in. slot.

The phenomenon of overblowing can be avoided by limiting the jet exit pressure to 1.5 times the local static pressure in the slot region. This can be accomplished at high jet mass flow rates by increasing the area of the slot. At the high blowing rates, the larger area of the 24-3 in. slot is beneficial (Fig. 47b), since a lower jet total pressure is required to obtain a given MFR (Table 1). Overblowing starts at MFR = 0.12 x 10^{-3} for the 16-11 in. slot; for the 24-3 in. slot, the onset of overblowing does not occur until MFR = 0.24 x 10^{-3}. For both slot configurations, the computed results indicate that blowing can generate useful amounts of yawing moment at moderate blowing rates, even at transonic Mach numbers.

Force Onset Time Lag

Time-accurate solutions are obtained using the isolated F/A-18 forebody, the 16-11 in. slot configuration, and MFR = 0.06 x 10^{-3} to determine the force onset time lag associated with forebody tangential slot blowing. The forebody yawing-moment coefficients, C_n, are plotted against time, t, in Fig. 52. Blowing is activated at $t = 0.0$ in all cases. The time lag associated with charging up the plenum chamber or associated plumbing is not modeled. The yawing-moment coefficient time histories (Fig. 52) show that at $M_\infty = 0.243$, it requires about 0.15 seconds for the yawing moment to reach a maximum steady value. This value is consistent with data obtained in sub-scale[7] and full-scale[8] wind tunnel tests. As the freestream Mach number increases, the time lag decreases since it requires less time to convect disturbances downstream. In all cases, the flow field has reached its steady-state value in the time required for the freestream flow to traverse approximately three mean aerodynamic chord lengths, which corresponds to the length of the isolated forebody used in the present computations.

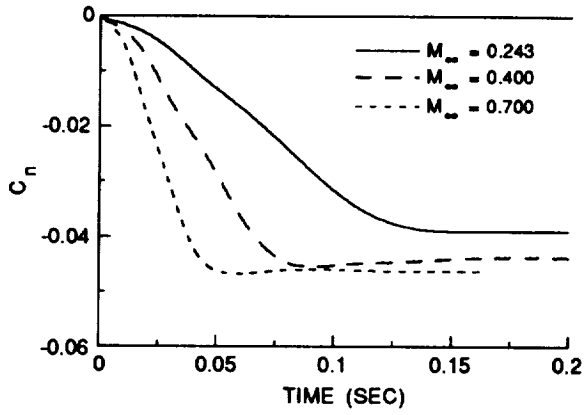

Fig. 52. Time history of forebody yawing moment. $M_\infty = 0.243$, $\alpha = 30.3°$, $Re_{\bar{c}} = 11.0 \times 10^6$, MFR = 0.06×10^{-3}, 16-11 in. slot.

The time lag is also studied by examining the surface-pressure coefficient at two axial locations on the forebody barrel (Fig. 53). The two points are located on the forebody barrel on the blowing side of the body, as shown in Fig. 54. At F.S. 142, for $M_\infty = 0.243$ (Fig. 53a), the computed data shows a delay of about 0.01 seconds, followed by a ramp down of the surface pressure over a period of 0.065 seconds. This behavior is also seen in the experimental data.[8] As the freestream Mach number increases, the response time decreases. At F.S. 184 (Fig. 53b), the response times increase to 0.025 seconds and 0.075 seconds for the delay and ramp down, respectively. Again, the response time decreases with increasing Mach number. This data indicates that the time lags associated with development of yawing moments using pneumatic slot blowing for forebody flow control are not large enough to be detrimental to the usefulness of the system.

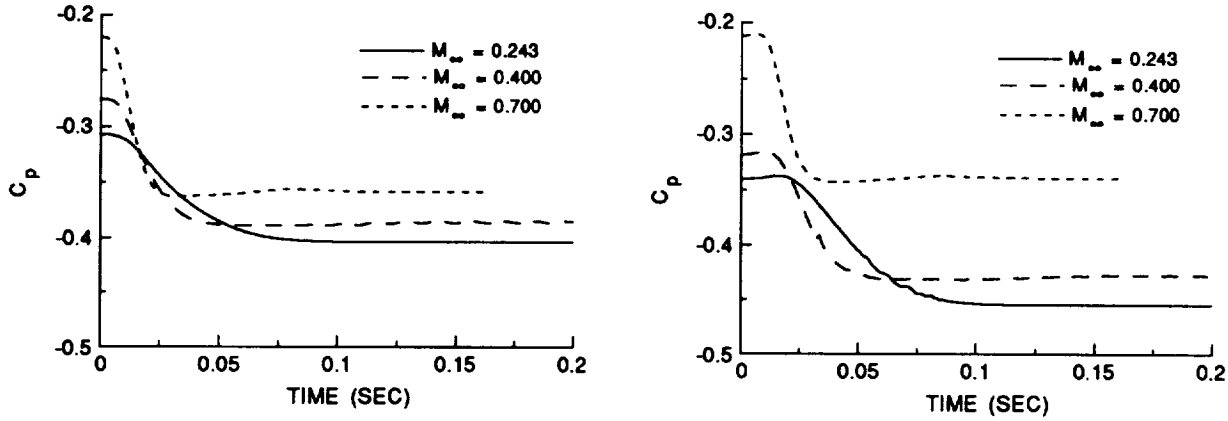

a) F. S. 142, $\phi = 240°$

b) F. S. 184, $\phi = 240°$

Fig. 53. Time history of surface pressure coefficient. $M_\infty = 0.243$, $\alpha = 30.3°$, $Re_{\bar{c}} = 11.0 \times 10^6$, MFR = 0.06×10^{-3}, 16-11 in. slot.

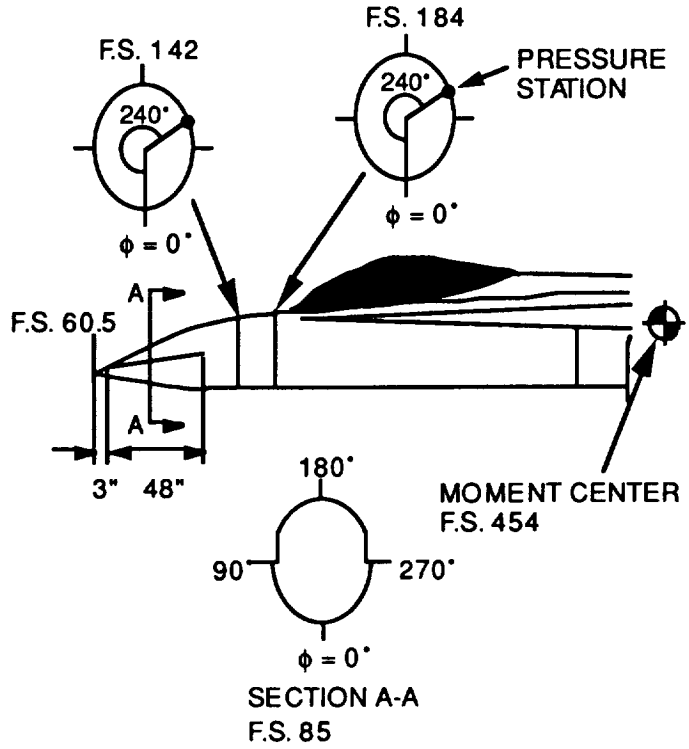

Fig. 54. Location of pressure stations used in surface pressure time history.

Conclusions

A computational study of forebody tangential slot blowing on an HARV geometry was carried out in four phases. In the first phase, various slot geometries were analyzed to determine the characteristics of an efficient slot geometry. The effect of sideslip on the efficiency of forebody tangential slot blowing was also studied. In the second phase, a computation was obtained at wind tunnel test conditions for comparison with available experimental data. This determined the ability of the numerical method to accurately model the flow field. The third phase consisted of computations using a model of the full HARV geometry. The solutions provided a detailed analysis of the effect of blowing on the flow field and the aerodynamic loads on the twin vertical tails. The final phase investigated the effect of freestream Mach number on the ability of forebody tangential slot blowing to generate yawing moment on the HARV isolated forebody. Force onset time lag of blowing was also studied on the forebody at various freestream Mach numbers.

The isolated HARV forebody was used for the first part of the study. a patched grid system was used to model the forebody and the slot was modeled as an actuator plane. It was found that a short slot placed close to the nose yielded the most side force and yawing moment per unit momentum blowing coefficient. Solutions with a sideslip angle of -10° were also obtained. Analysis of these solutions showed that the blowing system generated incremental changes in the side force and yawing moment on order with that obtained from the no-sideslip cases. The results indicate that the interaction of the jet separation vortex

with the LEX primary vortices played an important part in the generation of side force and yawing moments.

An isolated forebody computation with blowing was carried out at wind-tunnel test conditions, and compared with experiment. Comparisons were made between the computed and measured surface pressure coefficient. In general, the computed and measured flows were in good agreement, but discrepancies were observed in the jet separation location. The computational results indicate the jet to be attached for a greater distance than that inferred from the experimental data. However, no experimental flow visualization of the separation line was obtained. These discrepancies are believed to be the result of the eddy viscosity model employed in the jet region. However, the surface pressure coefficients in the jet region agreed fairly well with the experimental data. The results indicate the numerical method can be used to predict the performance of forebody tangential slot blowing with a fair degree of accuracy.

The effect of slot location on the efficiency of forebody tangential slot blowing on the HARV was analyzed using two non-time-accurate, full aircraft computations. One slot geometry consisted of a 16-in. active slot located 3 inches from nose, while the other had a 16-in. active slot located 11 inches from the nose. Solutions were obtained using flight conditions and a mass flow ratio corresponding to a wind-tunnel experimental value. Blowing from the 16-11 in. slot generated slightly greater local yawing moment in the slot region and over the LEX than similar blowing from the 16-3 in. slot. However, the total aircraft yawing moment coefficient generated by both slots at flight-test conditions (and identical mass flow ratios) were essentially the same. This result confirms the trend found in the full-scale wind tunnel data measured at maximum tunnel velocity.

The computations indicated a large interaction between the forebody and LEX flows and flow over the aft end of the aircraft. This showed the necessity of using full aircraft computations to predict the total yawing moment due to blowing, even though isolated forebody computations resolved the local forebody effects accurately. The blowing-side LEX vortex burst point moved forward due to blowing, while the non-blowing-side LEX vortex moved aft. Furthermore, the flow aft of the LEX vortex burst has been shown to be unsteady in both experimental and computational studies. In the present computations, the normal force coefficient was shown to converge to a steady value, whereas the side force coefficient fluctuated. This was due to the interaction of the unsteady flow field with the twin vertical tails.

The unsteadiness of the flow aft of the LEX vortex burst was analyzed by computing a time-accurate solution using the 16-11 in. slot geometry. The total yawing moment was found to be oscillatory and dependent on the local yawing moment contribution of the vertical tails. The average aircraft yawing moment agreed fairly well with experimental measurements, lending support to the use of the mass flow ratio as a correlating parameter. A Fast Fourier Transform analysis of the aerodynamic loads causing bending moment on the vertical tails yielded a dominant frequency slightly lower than that obtained from previous no-blowing computations, although the flow over the blowing-side vertical tail still contains a frequency peak within the natural frequency range of the vertical tails. This indicated that forebody tangential slot blowing had an effect on the frequency content of the flow, which in turn would affect tail buffet.

A computational analysis of the effect of freestream Mach number on the effectiveness of forebody tangential slot blowing was performed. Solutions were obtained at three different freestream Mach numbers. At each Mach number, two slot geometries and five different mass flow ratios were used. Additional solutions were obtained at the lowest freestream

Mach number using an even lower mass flow ratio. Time-accurate solutions were obtained to determine the force onset time lag due to blowing.

The computational results indicated that forebody tangential slot blowing remained effective, even at transonic Mach numbers. At the very low mass flow ratios, blowing had no effect on the flow field. The jet separated along the primary separation line seen in the no-blowing solution, and did not change the position of the forebody vortices. As the mass flow ratio increased, the yawing moment generated increased. At a given mass flow ratio, the yawing moment increased with increasing freestream Mach number. This was due to the increase in the jet exit velocity. As the jet exit velocity became sonic, this effect diminished. Further increases in the mass flow ratio lead to overblowing. This was especially evident at the highest freestream Mach number and highest MFR value analyzed. Overblowing was caused by the jet being underexpanded as it left the slot. The rapid expansion of the jet caused the jet to separate from the surface. This early separation reduced the effectiveness of the pneumatic system. Unlike the low blowing rate cases, the overblown jet still had an effect on the position of the vortices and generated a significant yawing moment. Overblowing was avoided by limiting the jet exit pressure ratio. For high jet mass flow rates, this was achieved by increasing the slot area. The results showed that tangential slot blowing remained effective at transonic Mach numbers.

Time-accurate solutions were obtained using one of the slot configurations, one mass flow ratio, and all three freestream Mach numbers. The yawing moment time history and the surface pressure coefficient time history at two points on the forebody barrel were recorded for each case. The yawing moment history indicated that a steady-state value was reached in the time required for a particle in the flow field to travel approximately three mean aerodynamic chord lengths. The surface pressure coefficient indicated a small delay followed by a ramp down in pressure as the jet was convected downstream. These time lags were of the same order as those measured in full-scale and sub-scale wind tunnel tests. The results indicated that the time lags did not present an obstacle to implementation of forebody tangential slot blowing on an aircraft.

The results of the computational analysis of forebody tangential slot blowing indicates that it is a viable method of producing side force and yawing moment on aircraft with long forebodies, such as the F/A-18. These results may be used to develop a practical system that can be installed on aircraft to provide additional control power while flying in the high-angle-of-attack regime. By thoroughly understanding the physics involved in tangential slot blowing, the efficiency of the system may be improved. The computational results, in conjunction with experimental data, provides such an understanding of the physics of forebody tangential slot blowing.

References

1. Del Frate, J. H., Fisher, F. D., and Zuniga, F. A., "In-Flight Flow Visualization with Pressure Measurements at Low Speeds on the NASA F-18 High Alpha Research Vehicle," NASA TM 101726, 1990.

2. Meyn, L. A. and James, K. D., "Full-Scale High Angle-of-Attack Tests of an F/A-18," AIAA Paper 92-2676, June, 1992.

3. Rizk, Y. M., Schiff, L. B., and Gee, K., "Numerical Simulation of the Viscous Flow Around a Simplified F/A-18 at High Angles of Attack," AIAA Paper 90-2999, 1990.

4. Rizk, Y. M. and Gee, K., "Unsteady Simulation of the Viscous Flowfield Around F-18 Aircraft at Large Incidence," *Journal of Aircraft*, Vol. 29, No. 6, November-December, 1992, pp. 986-992.

5. Ng, T. T. and Malcolm, G. N., "Aerodynamic Control Using Forebody Blowing and Suction," AIAA Paper 91-0619, January, 1991.

6. Ng, T. T., Suarez, C. J., and Malcolm, G. N., "Forebody Vortex Control Using Slot Blowing," AIAA Paper 91-3254-CP, September, 1991.

7. Kramer, B., Suarez, C., and Malcolm, G., "Forebody Vortex Control with Jet and Slot Blowing on an F/A-18," AIAA Paper 93-3449, August, 1993.

8. Lanser, W. R., Meyn, L. A., and James, K. D., "Forebody Flow Control on a Full-Scale F/A-18 Aircraft," AIAA Paper 92-2674, June, 1992.

9. Lanser, W. R. and Murri, D. G., "Wind Tunnel Measurements on a Full-Scale F/A-18 with Forebody Slot Blowing or Forebody Strakes," AIAA Paper 93-1018, February, 1993.

10. Steger, J. L., Ying, S. X., and Schiff, L. B., "A Partially Flux-Split Algorithm for Numerical Simulation of Compressible Inviscid and Viscous Flow," Proceedings of a Workshop on computational Fluid Dynamics, University of California, Davis, 1986.

11. Ying, S. X., Schiff, L. B., and Steger, J. L., "A Numerical Study of Three-Dimensional Separated Flow Past a Hemisphere Cylinder," AIAA Paper 87-1207, June, 1987.

12. Cummings, R. M., Rizk, Y. M., Schiff, L. B., and Chaderjian, N. M., "Navier-Stokes Predictions for the F-18 Wing and Fuselage at Large Incidence," *Journal of Aircraft*, Vol. 29, No. 4, 1992, pp. 565-574.

13. Baldwin, B. and Lomax, H., "Thin-Layer Approximation and Algebraic Model for Separated Turbulent Flows," AIAA Paper 78-0257, January, 1978.

14. Degani, D. and Schiff, L. B., "Computation of Turbulent Supersonic Flows About Pointed Bodies Having Crossflow Separation," *Journal of Computational Physics*, Vol. 66, No. 1, 1986, pp. 183-196.

15. Tavella, D. A., Schiff, L. B., and Cummings, R. M., "Pneumatic Vortical Flow Control at High Angles of Attack," AIAA Paper 90-0098, 1990.

16. Murman, S. M., Rizk, Y. M., Cummings, R. M., and Schiff, L. B., "Computational Investigation of Slot Blowing for Fuselage Forebody Flow Control," AIAA Paper 92-0020, 1992.

17. Benek, J. A., Steger, J. L., Dougherty, F. C., and Buning, P. G., "Chimera: A Grid Embedding Technique," AEDC-TR-85-64, Arnold Air Force Station, Tennessee, 1986.

18. Steger, J. L. and Rizk, Y. M., "Generation of Three-Dimensional Body-Fitted Coordinates Using Hyperbolic Partial Differential Equations," NASA TM 86753, 1985.

19. Degani, D. and Zilliac, G. G., "Experimental Study of the Non-steady Asymmetric Flow Around an Ogive-Cylinder at Incidence," *AIAA Journal*, Vol. 28, No.4, 1990, pp. 642-649.

20. Degani, D. and Schiff, L. B., "Numerical Simulation of the Effect of Spatial Disturbances on Vortex Asymmetry," *AIAA Journal*, Vol. 29, No. 3, 1991, pp. 344-352.

21. Degani, D., "Numerical Investigation of the Origin of Vortex Asymmetry," AIAA Paper 90-0593, 1990.

22. Levy, Y., Degani, D., and Seginer, A., "Graphical Visualization of Vortical Flows by Means of Helicity," *AIAA Journal*, Vol. 28, No. 8., 1990, pp. 1347-1352.

23. Font, G. I. and Tavella, D. A., "High Alpha Aerodynamic Control by Tangential Fuselage Blowing," *AIAA Journal*, Vol. 30, No. 5, 1992, pp. 1321-1330.

24. Font, G., "Force Production Mechanisms of a Tangential Jet on Bodies at High Alpha," AIAA Paper 92-4648, 1992.

25. LeMay, S. P., Sewall, W. G., and Henderson, J. F., "Forebody Vortex Flow Control on the F-16C Using Tangential Slot and Jet Nozzle Blowing," AIAA Paper 92-0019, 1992.

26. Guyton, R. W. and Maerki, G., "X-29 Forebody Jet Blowing," AIAA Paper 92-0017, 1992.

27. Rizk, Y., Guruswamy, G., and Gee, K., "Numerical Investigation of Tail Buffet on F-18 Aircraft," AIAA Paper 92-2673, 1992.

28. Martin, C. A. and Thompson, D. H., "Scale Model Measurements of Fin Buffet Due to Vortex Bursting on F/A-18," AGARD Fluid Dynamics Specialists Meeting, Paper 12, 1991.

29. Meyn, L. N. and Ross, J. C., Private communications, 1991.

30. Del Frate, J. H., Freudinger, L. C., and Kehoe, M. W., "F-18 Tail Buffet," High Angle of Attack Technology Program Workshop, 1989.

31. Bean, D. E. and Wood, N. J., "An Experimental Investigation of Twin Fin Buffeting and Suppression," AIAA Paper 93-0054, 1993.

32. Erickson, G. E., "Wind Tunnel Investigation of Vortex Flows on F/A-18 Configuration at Subsonic Through Transonic Speeds," NASA Technical Paper 3111, December, 1991.

Appendix A

Publications made under grant NCC2-657

1. Gee, K., Rizk, Y. M., and Schiff, L. B., "Analysis of Tangential Slot Blowing on F/A-18 Isolated Forebody," 12th Applied Aerodynamics Conference, June 20-23, 1994, AIAA Paper 94-1831.

2. Gee, K., Rizk, Y. M., and Schiff, L. B., "Effect of Forebody Tangential Slot Blowing on Flow about a Full-Aircraft Geometry," 24th Fluid Dynamics Conference, July 6-9, 1993, AIAA Paper 93-2962.

3. Gee, K., Tavella, D., and Schiff, L. B., "Computational Investigation of a Pneumatic Forebody Flow Control Concept," *Journal of Aircraft*, Vol. 30, No. 3, May-June 1993, pp. 326-333.

4. Gee, K., Rizk, Y. M., Murman, S. M., Lanser, W. R., Meyn, L. A., and Schiff, L. B., "Analysis of a Pneumatic Forebody Flow Control Concept About a Full Aircraft Geometry," 10th Applied Aerodynamics Conference, June 22-24, 1992, AIAA Paper 92-2678.

5. Gee, K. and Murman, S. M., "Computational Simulation of Flow over the F-18 HARV at Large Incidence," NASA High-Angle-of-Attack Projects and Technology Conference, Edwards, CA, April 21-24, 1992.

6. Gee, K., Tavella, D., and Schiff, L. B., "Computational Optimization of a Pneumatic Fuselage Forebody Flow Control Concept," 9th Applied Aerodynamics Conference, September 23-25, 1991, AIAA Paper 91-3249.